chemistry

MDPI

Article

Targeted Drug Delivery of Anticancer Agents Using C_5N_2 Substrate: Insights from Density Functional Theory

Syeda Huda Mehdi Zaidi [1], Muhammad Ajmal [1], Muhammad Ali Hashmi [1,2,*] and Ahmed Lakhani [3,*]

[1] Department of Chemistry, Division of Science & Technology, University of Education, Lahore 54770, Pakistan; syedahudamehdi@gmail.com (S.H.M.Z.); majmal@ue.edu.pk (M.A.)
[2] School of Chemical and Physical Sciences, Victoria University of Wellington, Wellington 6012, New Zealand
[3] Department of Biomedical and Health Sciences, Calumet College of St. Joseph, 2400, New York Ave, Whiting, IN 46394, USA
* Correspondence: muhammad.hashmi@ue.edu.pk (M.A.H.); alakhani@ccsj.edu (A.L.)

Abstract: Cancer has a threatening impact on human health, and it is one of the primary causes of fatalities worldwide. Different conventional treatments have been employed to treat cancer, but their non-specific nature reduces their therapeutic efficacy. This study employs a C_5N_2-based targeted drug carrier to study the delivery mechanism of anticancer drugs, particularly cisplatin, carmustine, and mechlorethamine, using density functional theory (DFT). The geometries of the drugs, the C_5N_2 substrate, and the drug@C_5N_2 complexes were optimized at the PBE0-D3BJ/def2SVP level of theory. Interaction energy was computed for the complexes which follow the trend, i.e., cisplatin@C_5N_2 (-27.60 kcal mol^{-1}) > carmustine@C_5N_2 (-19.69 kcal mol^{-1}) > mechlorethamine@C_5N_2 (-17.79 kcal mol^{-1}). The non-covalent interaction (NCI) and quantum theory of atoms in molecules (QTAIM) analyses confirmed the presence of van der Waals forces between the carmustine@C_5N_2 and mechlorethamine@C_5N_2 complexes, while weak hydrogen bonding has also been observed between the cisplatin@C_5N_2 complex. Electron localization function (ELF) analysis was performed to analyze the degree of delocalization of electrons within the complexes. The electronic properties of the analytes and the C_5N_2 substrate confirmed the enhanced reactivity of the complexes and illustrated electron density shift between the drugs and the C_5N_2 sheet. Recovery time was determined to assess the biocompatibility and the desorption behavior of the drugs. Moreover, negative solvation energies and increased dipole moments in a solvent phase manifested enhanced solubility and easy circulation of the drugs in biological media. Subsequently, this study illustrates that cisplatin@C_5N_2, carmustine@C_5N_2, and mechlorethamine@C_5N_2 complexes can be utilized as efficient drug delivery systems.

Keywords: density functional theory; anticancer; drug delivery; interaction energy; electronic properties; therapeutic; substrate

check for updates

Academic Editor: Alessandro Ponti

Received: 29 April 2025
Revised: 10 June 2025
Accepted: 12 June 2025
Published: 13 June 2025

Citation: Mehdi Zaidi, S.H.; Ajmal, M.; Hashmi, M.A.; Lakhani, A. Targeted Drug Delivery of Anticancer Agents Using C_5N_2 Substrate: Insights from Density Functional Theory. *Chemistry* **2025**, *7*, 98. https://doi.org/10.3390/chemistry7030098

Copyright: © 2025 by the authors. Licensee MDPI, Basel, Switzerland. This article is an open access article distributed under the terms and conditions of the Creative Commons Attribution (CC BY) license (https://creativecommons.org/licenses/by/4.0/).

1. Introduction

Over the past few years, cancer has adversely affected human health and caused millions of deaths worldwide [1,2]. Various conventional approaches, including surgical treatment [3], radiation therapy [4], and chemotherapy [5] have been considered definitive solutions for cancer treatment. However, their non-specific nature and cytotoxicity further minimize their pharmacological effects [6–8]. Cisplatin (cis-diamminedichloroplatinum (II)) [9] is the most widely used anticancer drug to treat various types of malignancies related to the head, neck [10], ovaries [11], and bladder [12]. It forms an adduct with DNA,

inhibiting its replication further and causing cell death [13]. Moreover, its therapeutic efficiency has been validated with various drug delivery systems, including selenium nanoparticles, to treat lung carcinoma [14]. It has also been delivered using polypeptide vesicles [15], magnetic iron oxide nanoparticles [16], and graphitic carbon nitride-based drug delivery systems [17]. Carmustine (BCNU), an alkylating agent commonly known as 1,3-bis (2-chloroethyl)-1-nitrosourea [18], has been popular in cancer treatment [19]. Its efficiency has been investigated for curing and suppressing brain tumors such as glioblastoma multiforme [20] using substrates such as polymeric nanoparticles [21] and polyamidoamine (PAMAM) dendrimers [22]. Also, its interaction with chitosan-coated nanoparticles was evaluated and approved to cure brain-associated tumors [23]. Recently, carmustine has been used for the treatment of ovarian cancer, employing a liposomal substrate [24]. Its therapeutic efficacy has also been reported with carbon and boron nitride nanotubes [25] to treat malignant cancers. Consequently, mechlorethamine (mustine), an anticancer medication, has been employed to cure Hodgkin's lymphoma [26] and cutaneous T-cell lymphomas [27,28]. Its anticancer efficacy has been investigated with nanocages, including silicon, carbon, and aluminum nitride [29]. However, severe health problems have been associated with the delivery of these anticancer drugs as they lack precision in differentiation between cancerous and healthy cells [30]. Moreover, anticancer drugs can cause serious health problems, mainly cell toxicity, due to their non-specific interaction, further minimizing their remedial efficacy [31,32]. Therefore, support systems have been evaluated for their controlled and direct release at the cancerous site to overcome associated health complications [33,34]. The drug carriers facilitate the medications to cross complex biological defense systems without causing widespread malignancies [35]. Theoretical [36] and experimental [37] evaluations of the drugs with different carriers have also been performed to enhance the cell targeting and bioimaging properties of anticancer drugs. Various two-dimensional (2D) [38,39], and three-dimensional (3D) [40,41] substrates have been examined, including hexagonal boron nitride (h-BN) [42], manganese dioxide [43], transition-metal di-chalcogenides (TMDs) [44], metallic nanoparticles [45], MXenes [46], and phosphorene [47], for the drug delivery. Additionally, nanocarriers comprising carbon have also been reported as potential drug carriers with low cytotoxicity and good chemical stability, i.e., chitosan [48], fullerene [49], and fluorinated graphene nanocarbon [50]. The reactivity of carbon nanotubes has been validated after encapsulation of an anticancer drug, i.e., cisplatin [51]. In some studies, preparation, and cytotoxicity of dendrimers [52] and liposomal complexes [53] conjugated with doxorubicin and cisplatin have also been examined to improve the cellular uptake of the drugs. Comparatively, carbon nitride offers more benefits in the targeted delivery of anticancer drugs because of its distinctive physicochemical characteristics [54,55].

Different experimental and theoretical studies have been performed on the drug delivery efficiency of carbon nitrides comprising different ratios of carbon and nitrogen such as CN [56], C_2N [57], and C_3N_4 [58,59] nanosheets. Recent studies on carbon nitrides manifest their suitable band gaps, which make them good photocatalysts for water splitting [60], CO oxidation [61], CO_2 reduction [62], H_2O_2 production [63], and nitrogen reduction reaction [64,65]. Furthermore, graphitic carbon nitride g-C_3N_4 has been reported as an efficient substrate for delivering carboplatin [66], and melphalan [67] to treat malignant tumors. Significant stability [68], pH sensitivity [69], and photoluminescence [70] of carbon nitrides have been revealed which make them capable of delivering anticancer drugs such as lonidamine [71], flutamide [72], and cisplatin at the cancerous site. Among carbon nitrides, C_5N_2 is a nitrogen-rich covalent carbon nitride with a stoichiometric ratio of five carbon to two nitrogen atoms. It has shown promising structural and electronic properties suitable for drug delivery and emerged as a novel biocompatible substrate with a narrow band gap

of 1.10 eV. It has a substantial drug-loading rate because of micropore abundance and large surface area [73].

Recent studies have explored a range of nanomaterials such as carbon nanotubes (CNTs) [74], mesoporous silica [75], and metal–organic frameworks [76] as drug delivery vehicles, due to their high surface area and tunable surface chemistry. However, many of these systems face limitations like potential cytotoxicity and limited biodegradability. In contrast, C_5N_2 is a nitrogen-rich carbon material with various favorable properties. Its conjugated framework provides strong interactions including π–π stacking, hydrogen bonding, and van der Waals forces with drug molecules, while nitrogen in-corporation enhances its potential for targeted functionalization and improves bio-compatibility compared to carbon-based carriers like graphene oxide [77]. Unlike metal-based carriers that cause long-term toxicity [78], C_5N_2 is metal-free and potentially less immunogenic. Moreover, its stable structure and ease of synthesis through a condensation reaction between 1,2,4,5-benzene tetramine and hexaketocyclohexane make it a promising platform that overcomes several disadvantages of currently used systems [79]. Moreover, some studies have demonstrated the potential of C_5N_2 in drug delivery [80,81] in which carbon nitride nanoparticles have been experimentally evaluated to deliver doxorubicin, hydroxycamptothecine, and propidium iodide to the nucleus via endosomal escape facilitated by functional groups [82]. It demonstrated its efficient intracellular transport and therapeutic potential. These combined advantages justify C_5N_2 as a safer, more tunable, and effective drug delivery system [83]. Hence, these inspiring properties and results encouraged us to explore and evaluate the theoretical efficiency of the C_5N_2 carrier to deliver anticancer drugs, mainly cisplatin, carmustine, and mechlorethamine at the tumor site. In this work, DFT calculations were performed to assess the interaction between the drugs and the substrate in both the gas and the solvent media. The intermolecular interactions between cisplatin@C_5N_2, carmustine@C_5N_2, and mechlorethamine@C_5N_2 were evaluated using NCI, QTAIM, and ELF analyses. To ensure efficient and controlled drug release at the targeted site, evaluation of the interaction between the drugs and the C_5N_2 substrate was carried out through FMO, DOS, NBO, and EDD analyses. Moreover, the reactivity, stability, and binding affinity of the complexes were analyzed through chemical reactivity descriptors.

2. Computational Methodology

Structures of the cisplatin, carmustine, mechlorethamine, C_5N_2 substrate, and their complexes were modeled and visualized utilizing the Gauss View program [84,85]. Computational calculations of different configurations of the drugs and the C_5N_2 carrier were performed using DFT (density functional theory) employing Gaussian 16 rev.C.01 software [86] at the PBE0-D3BJ/def2-SVP level of theory. PBE0 is a hybrid density functional preferred for the optimization of various structures such as analytes anchored two-dimensional supports [87]. Also, it provides a more accurate illustration of the molecular characteristics and electronic structures of various materials, including solids, organic molecules, and complexes of metals and non-metals [88]. It addresses the restrictions of pure density functional theory approximations and accurately predicts the structural and electronic properties of the molecules across the periodic table [89]. It provides significant estimations for the systems exhibiting non-covalent interactions, electronic excitations, and electron density shifts. Moreover, it is commonly employed in various fields, including drug delivery, to simulate optimizations and binding energy calculations [90,91]. Also, structural, optical, and vibrational properties of graphitic carbon nitrides [92] along with efficient hydrogen storage [93] were studied using PBE0 functional.

Different studies have highlighted its efficiency in predicting molecular phenomena, such as the photoisomerization of unsubstituted spirooxazine [94]. It has also been em-

ployed to deliver anticancer drugs, mainly hydroxyurea [95] and cisplatin [96], through borospherenes and metallacage drug delivery systems, respectively. It is scrutinized to study the charge transfer mechanism of phosphorus, oxygen, and sulfur-doped graphitic carbon nitride [97]. Interpretation of adsorption and separation phenomena of NO and CO_2 over the surface of the C_5N_2 substrate has been computed at this hybrid functional. Adsorption of metformin [98], CO_2, and CH_4 [99] on functionalized C_3N_4 have also been validated using PBE0. It has been used to investigate the adsorption mechanism of H_2, N_2, CO, NH_3, H_2S, and SO_2 [100], and modifications of electronic properties in platinum and silicon-doped C_3N_4 have also been investigated [101]. Evaluation of CO_2 reduction on copper [102] and analysis of electronic properties on Zn/Ga doped C_3N_4 [103] have also been computed. The PBE0-D3BJ functional was selected due to its reliable performance in modeling noncovalent interactions such as van der Waals forces and hydrogen bonding, which are key factors for the adsorption of drugs. The def2-SVP basis set offers a good balance between accuracy and computational cost. This level of theory has been successfully applied in similar drug delivery studies involving carbon-based and nitrogen-rich nanomaterials [104,105]. Stefan Grimme's empirical dispersion correction (D3 correction) with Becke Johnson damping (D3-BJ) [106] has been utilized to correct the energies for non-bonding interactions within the molecular system. The accuracy of this method in describing the structural and molecular variations in non-covalent systems has also been reported in the literature [107]. For solvent based calculations, SMD solvation model was employed at the same level of theory using water as a solvent. CYLview software was used to obtain and visualize detailed and precise portraits of the drug@C_5N_2 complexes [108]. Geometry optimization was carried out using the simulated structure of the C_5N_2 sheet. A variety of possible orientations were considered to determine the stable arrangement of the drug on the C_5N_2 surface. Following optimization, vibrational frequency analysis was performed on the structures to confirm their minimal energy configurations on the potential energy surface. Interaction energy (E_{int}), a significant parameter, was obtained to evaluate the interaction between the drug and the C_5N_2 surface within the complex using the following expression:

$$\Delta E_{int} = [E_{drug@C_5N_2} - \left(E_{drug} + E_{C_5N_2}\right)] \quad (1)$$

The interaction energy of the drug@C_5N_2 system is represented by E_{int}, where $E_{drug@C_5N_2}$, E_{drug}, and $E_{C_5N_2}$ represent the interaction energies of the complex, the drug, and the C_5N_2 sheet, respectively [109]. Non-covalent interactions (NCI) analysis, also known as the reduced density gradient (RDG) method, was performed to analyze the weak interactions between the drug and the C_5N_2 substrate using Multiwfn [110] and visual molecular dynamics (VMD) [111] programs. Electron density (ρ) and reduced density gradient(s) are the two key derivatives used to analyze interactions such as stearic repulsions, van der Waals interactions, and hydrogen bonding between the complexes. The RDG is a dimensionless gradient norm function, and it is inversely related to the electron density (ρ). Moreover, it identifies the regions of non-covalent interactions with relatively low electron densities. Mathematically, RDG (s) is expressed as [112]

$$RDG(s) = \frac{1}{2(3\pi^2)^{\frac{1}{3}}} \frac{\nabla\rho}{\rho^{\frac{4}{3}}} \quad (2)$$

The magnitude of electronic density plays a significant role in determining the strength of non-covalent interactions. According to the equation, the greater value of RDG further decreases the electronic density suggesting a minimal possibility of non-covalent interaction. Comparatively, the lower value of RDG enhances the potential of non-covalent interactions

by increasing the electronic density at a particular site of interaction. The attractive and repulsive nature of interaction and spatial distribution of electron density is determined by the Laplacian of electronic density $(\nabla^2\rho)$. Also, it provides necessary information about the electron-rich and electron-depleted regions. A negative value $(\nabla^2\rho < 0)$ illustrates the region of concentrated electronic density, confirming the formation of covalent bonds. Moreover, the positive value $(\nabla^2\rho > 0)$ corresponds to the depletion of electronic density as found in van der Waals interactions. Mathematically, $(\nabla^2\rho)$ is expressed as a trace of the Hessian matrix of electronic density as shown below [113]:

$$\nabla^2\rho = \lambda_1 + \lambda_2 + \lambda_3 \quad (3)$$

Here $\lambda_1, \lambda_2, \lambda_3$ represents the eigenvalues of the Hessian matrix which assist in describing the behavior of interactions. Among these eigenvalues, λ_2 plays a crucial role in identifying the nature of interactions, i.e., $(\lambda_2 < 0)$ represents strong and attractive interaction, $(\lambda_2 > 0)$ corresponds to strain and stearic repulsion, and $(\lambda_2 = 0)$ predicts the presence of weak interactions such as van der Waals forces. To visualize and evaluate the type, strength, and spatial pattern of non-covalent interactions, we generated a 2D RDG scatter plot and a 3D isosurface representing interactions using Multiwfn and VMD software. The 2D graph combines the sign λ_2 with the electron density (ρ) to explain the type of interaction ranging from $(-0.05$ to $0.05)$. To augment the 2D scatter plot, the 3D isosurface is represented by the colors of the sign of λ_2, i.e., blue color indicates the presence of strong and attractive interactions illustrated by the region where $(\text{sign}(\lambda_2)\rho < 0)$, red color represents repulsive stearic interactions indicated by $(\text{sign}(\lambda_2)\rho > 0)$, and green corresponds to the weak van der Waals interactions as illustrated by $(\text{sign}(\lambda_2)\rho = 0)$ on the x- axis of the 2D plot. The color representation facilitates a direct visualization of the interaction domains within the complex systems [114]. The nature of the interaction that exists during the complexation of the drug@C_5N_2 complex has also been visualized through the quantum theory of atoms in molecules analysis (QTAIM). It locates all the interactions among atoms by pairing up the densities of electrons spinning oppositely which further illustrate the non-covalent interactions within the complexes [115]. Topological analysis of the electronic density (ρ) is the foundation of atoms in molecules (AIM) analysis [116]. Further, it interprets the interactions between the drug@substrate complexes, i.e., cisplatin@C_5N_2, carmustine@C_5N_2, mechlorethamine@C_5N_2 through certain parameters including electronic density (ρ), the Laplacian of electronic density $(\nabla^2\rho)$, the total energy density (H), the potential energy density (V), and the kinetic energy density (G) computed at the bond critical points (BCPs) and the curvature of the bond. The strength of the non-covalent interaction is specified by the values of electronic density (ρ). If $(\rho > 0.1)$, it indicates the presence of intermolecular attractive forces, while $(\rho < 0.1)$ suggests the presence of van der Waals interactions between the drug@C_5N_2 complexes [117]. Overall energy distribution of the complex systems was evaluated through the total energy density (H), which is the sum of the potential (V) and kinetic (G) energy densities, and it is expressed as [118]

$$H(r) = V(r) + G(r) \quad (4)$$

The signs of the potential energy density (V) and the kinetic energy density (G) manifest coherency, with (V) being negative and (G) being positive. This notation is standard in quantum theory of atoms in molecules (QTAIM) and is widely used in studies involving topological analysis of electron density [119]. Moreover, the nature of the interactions between the drugs and the C_5N_2 sheet whether covalent or non-covalent have also been validated by analyzing the values of the key indicators such as Laplacian of electron density $(\nabla^2\rho)$ and energy density (H). Additionally, the greater value of $(\nabla^2\rho)$ and (H) mani-

fests the presence of non-covalent interactions between the drug and the C_5N_2 substrate, i.e., $(H > 0 < \nabla^2\rho)$. In contrast, drug@C_5N_2 complexes exhibit strong attraction when these parameters manifest a relation, i.e., $(\nabla^2\rho < 0)$, $(H < 0)$. Electronic properties of the drug@C_5N_2 complexes were computed through different analyses. Frontier molecular orbital (FMO) analysis was employed to analyze the electronic structure and charge transfer characteristics of the complexes mainly concentrating on the HOMO and LUMO molecular orbitals. For the C_5N_2 substrate, the drugs, and their complexes, calculations were performed to determine the energies of the HOMO and the LUMO. The energy of the highest occupied molecular orbital (HOMO) illustrates the electron donating capability (high value of E_{HOMO}), while the energy of the lowest unoccupied molecular orbital (LUMO) predicts the electron-accepting ability (high value of E_{LUMO}) of a molecule after the complex formation. E_{HOMO} represents the ionization potential (I) of the molecule and E_{LUMO} corresponds to the electron affinity (A) of the system. According to Koopman's theorem, FMOs are correlated with the (I) and (A) values by a relation, $(I = -E_{HOMO}, A = -E_{LUMO})$ [120].

Moreover, another parameter is the energy gap (E_g) between the HOMO and the LUMO of the complex system which provides significant insights into the adsorption behavior, reactivity, and stability of the drug at the C_5N_2 sheet. It is calculated using the expression, $(E_g = E_{LUMO} - E_{HOMO})$ where E_{LUMO} is the lowest energy level of the unoccupied molecular orbital and E_{HOMO} represents the highest energy level of the occupied molecular orbital. The global reactivity descriptors, including chemical potential (μ), electrophilicity index (ω), hardness (η), and softness (s), were computed from the energies of the HOMO and the LUMO at the same level of theory. The reactivity, stability, and the interaction behavior of the drugs at the C_5N_2 surface were analyzed by employing expressions [121],

$$\mu = -\left(\frac{I + E}{2}\right) \tag{5}$$

$$\omega = \frac{\mu^2}{2\eta} \tag{6}$$

$$\eta = \left(\frac{I - A}{2}\right) \tag{7}$$

$$S = \frac{1}{2\eta} \tag{8}$$

(μ) is related to the electronegativity of the molecule and its more negative value depicts the difficulty in the removal of an electron showing less reactivity with higher stability. (ω) provides insight into the stabilization energy acquired after fulfilling the electrons (gained from the surrounding environment) [122]. A lower value of (ω) corresponds to the nucleophilicity of a molecule (acts as a nucleophile) while its higher value depicts electrophilicity of a molecule (acts as an electrophile). The values of (η) and (S) significantly play their role in the evaluation of the polarizability of the chemical system, i.e., a small energy gap corresponds to a soft molecule (high polarizability), while a large energy gap is related to a hard molecule (less polarizability) [123]. The density of states (DOS) justifies the FMO analysis by providing a comprehensive view of the energy gap and the electronic properties of the complexes. Evaluation of the orbitals was performed by the FMO analysis while the states of electron density near the HOMO−LUMO gap (E_{H-L} gap) were analyzed through DOS using the GaussSum program [124]. Moreover, electron localization function (ELF) analysis has also been carried out to understand the weak interactions, including van der Waals forces, by visualizing electron density changes after the formation of a complex [125]. ELF measures the extent of electron density localization, i.e., $(ELF \approx 1)$ refers to high electron localized regions which indicates the presence of covalent bond,

(ELF ≈ 0.5) refers to electron delocalized regions indicating the presence of non-covalent interactions, and (ELF ≈ 0) highlights the non-interacting regions with minimum electron density [126]. We generated color-coded ELF maps to analyze and distinguish between the localized (covalent) and delocalized (non-covalent) interactions between the drug@C_5N_2 complexes through Multiwfn v. 3.0.8 program. Natural bond orbital (NBO) analysis is used to analyze the electronic density shifts between the complexes [127]. Also, it helps in identifying the charge transfer mechanism between the donor and the acceptor sites within the drug@C_5N_2 complexes. Electron Density Distribution (EDD) analysis provides insights into the charge distribution between atoms within the molecular system [128]. We have visualized the flow of electrons by analyzing the electron density changes after the association of the drug@C_5N_2 system.

3. Results and Discussion

C_5N_2 is a porous crystalline structure with five fused benzene rings comprising two types of C-C bonds having bond lengths, i.e., 1.42 Å and 1.37 Å. Each benzene ring is bridged by a pyrazine ring which constitutes C-N and C-C bond with bond lengths 1.36 Å and 1.39 Å, respectively. Different orientations of the drugs (cisplatin, carmustine, and mechlorethamine) were considered at different locations on the C_5N_2 sheet to determine the most stable configuration of the complex. The spatial distinction of these binding sites can easily be evaluated through their designations such as (a) located in the central cavity of the sheet, (b) positioned directly above the benzene ring, (c) located above the pyrazine ring, (d) aligned just above the hydrogenated benzene ring, and (e) forming a pseudo-cycle with the nitrogen and hydrogen atoms present at the inside edges of the sheet. The optimized sheet of C_5N_2 representing possible active sites is shown in Figure 1.

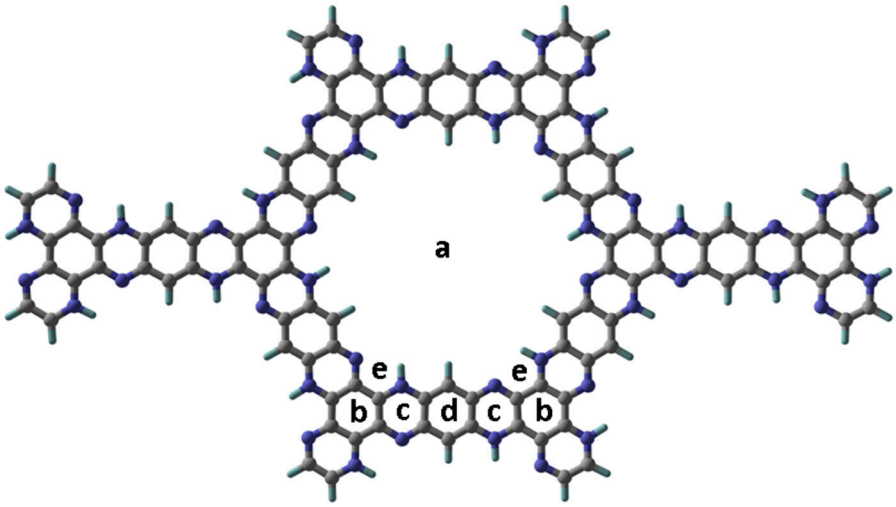


Figure 1. Optimized structure of the C_5N_2 sheet at PBE0-D3BJ/def2-SVP level of theory. The central cavity (a), benzene ring (b), pyrazine ring (c), hydrogenated benzene ring (d), and a pseudo-cyclic triazine (e) are highlighted as possible active sites of the C_5N_2 sheet. Gray, blue, and bluish white colors represent carbon (C), nitrogen (N), and hydrogen (H) atoms, respectively.

After examining different orientations and positions (see Figure S1), the most stable geometry of the cisplatin is observed over the benzene (b) and pyrazine ring (c) of the C_5N_2 sheet with an interaction energy of −27.60 kcal mol^{-1}. The two hydrogen atoms (H1 and H3) of the cisplatin drug interacted with the C2 and N4 of the C_5N_2 sheet while keeping a distance of 2.36 Å and 1.92 Å, respectively. The interaction between H1−C2 suggests the presence of van der Waals interaction while H3−N4 interacted with a relatively shorter distance which manifests the formation of a hydrogen bond (N−H−N) because it ranges

between (1.5 Å–2.0 Å) [129]. The platinum Pt5 is linked with the C6 of the C_5N_2 sheet with a bond distance of 3.39 Å and the two Cl atoms of the cisplatin (Cl7 and Cl9) show interaction with the C8 and C10 of the benzene ring of the C_5N_2 sheet with a highest bond length of 3.45 Å and 3.40 Å, illustrating van der Waals interaction between the cisplatin@C_5N_2 complex as shown in Figure 2 and Table 1.

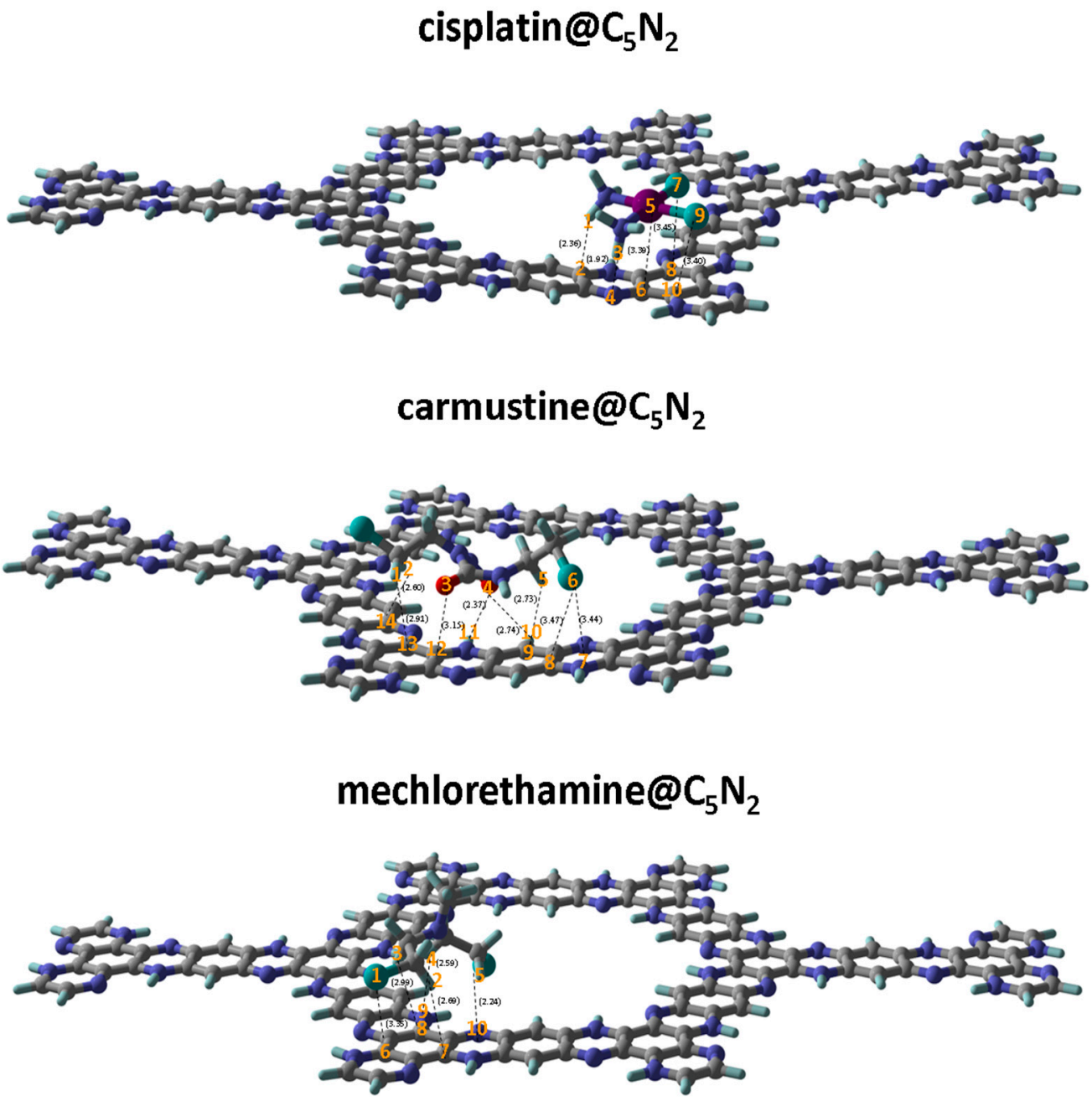


Figure 2. Stable geometries of the cisplatin@C_5N_2, carmustine@C_5N_2, and mechlorethamine@C_5N_2 complexes highlighting interacting atoms and their respective bond lengths (represented by spotted lines) between the drugs and the C_5N_2 sheet.

Table 1. Interaction energies (kcal mol^{-1}) with their corresponding bond lengths (Å) between the associated atoms of the drugs and the C_5N_2 carrier after complex formation.

Drug@C_5N_2 Complex	C_5N_2−Drug	Bond Lengths (Å)	Interaction Energy (kcal mol^{-1})
cisplatin@C_5N_2	C2−H1	2.36	−27.60
	N4−H3	1.92	
	C6−Pt5	3.39	
	C8−Cl7	3.45	
	C10−Cl9	3.40	
carmustine@C_5N_2	C13−H1	2.91	−19.69
	C14−H2	2.60	
	C12−O3	3.15	
	H11−O4	2.37	
	H10−O4	2.74	
	C9−H5	2.73	
	C8−Cl6	3.47	
	N7−Cl6	3.44	
mechlorethamine@C_5N_2	C6−Cl1	3.35	−17.73
	C7−H2	2.69	
	C8−H3	2.99	
	N9−H4	2.59	
	N10−H5	2.24	

For the carmustine drug, among different orientations (see Figure S2) the most suitable position is oriented parallelly above the sites (b), (c), and (d) of the C_5N_2 sheet with an interaction energy of −19.69 kcal mol^{-1}. The negative values of the interaction energy ensured the stability of the drug carriers. In addition, the hydrogen atoms, i.e., H10 and H11 of the C_5N_2 sheet interacted with O4 of the carmustine drug while maintaining a bond distance of 2.74 Å and 2.37 Å, respectively, which depicts the formation of a weak hydrogen bond between O4 and H11 of the complex. The bonding interactions with a distance of 2.73 Å, 2.91 Å, and 2.60 Å between H5−C9, H1−C13, and H2−C14 atoms, sequentially, indicate non-covalent interactions between the carmustine and the C_5N_2 sheet as they appear outside the normal range of a covalent bond (1.09 Å) [130]. The oxygen O3 interacted with C12 of C_5N_2 with a bond distance of 3.15 Å. Moreover, the chlorine (Cl6) atom of the carmustine exhibit interaction with N7 and C8 of the C_5N_2 sheet with a bond length of 3.44 Å and 3.47 Å, respectively, further suggesting van der Waals interaction as shown in Figure 2. For the mechlorethamine drug, among different feasible orientations (see Figure S3), the most stable configuration is attained at the top of the sites (b), (c), and (e). However, a chlorine atom (Cl1) of the drug is moved slightly and oriented above the pyrazine ring of the C_5N_2 sheet.

The suitable interaction energy of mechlorethamine complexed with the C_5N_2 is −17.73 kcal mol^{-1}. Hydrogen atoms (H2 and H3) of the drug exhibit non-covalent interaction with the C7 and C8 of the C_5N_2 sheet by keeping a distance of 2.69 Å and 2.99 Å. The H4 atom of the mechlorethamine drug is interacted with the N9 of the C_5N_2 sheet by 2.59 Å. Besides this, a distance of 2.24 Å is observed between H5 and N10 of the drug and the substrate complex. These bond lengths are outside the normal range of a covalent bond (1.01 Å) [131] and can be considered weak hydrogen bonds between N−H or van der Waals interactions (~ 2.0 Å to 3.5 Å) [132] between H−C atoms. Moreover, chlorine (Cl1) is also linked with the carbon (C6) of the C_5N_2 sheet while maintaining a bond distance of 3.35 Å, further confirming that Cl−C is connected through van der Waals interaction. Hence the negative values of the interaction energies and suitable bond distances manifested the

potential of cisplatin@C_5N_2, carmustine@C_5N_2, and mechlorethamine@C_5N_2 complexes to be evaluated as drug delivery systems.

The results of interaction energies manifested that the most stable geometry is identified for the cisplatin@C_5N_2 complex because of weak hydrogen bonding between the drug and the substrate. Additionally, the presence of two electron-rich oxygen atoms in the carmustine@C_5N_2 complex contributes to its relatively stronger adsorption on the surface of the C_5N_2 carrier as compared to mechlorethamine@C_5N_2 complex as shown in Table 1. Based on the calculated interaction energies and bond lengths, the adsorption strength follows the order: cisplatin@C_5N_2 > carmustine@C_5N_2 > mechlorethamine@C_5N_2, indicating that cisplatin exhibits the strongest binding affinity to the C_5N_2 substrate. The most suitable alignment and the position over the C_5N_2 sheet for cisplatin, carmustine, and mechlorethamine is represented in Figure 2. The resulting interaction energies of the complexes (drug@C_5N_2) with different orientations of the drugs over the substrate are presented in Table S1.

3.1. Topological Analysis

3.1.1. Non-Covalent Interaction (NCI) Analysis

NCI analysis was performed on the most stable complexes of the cisplatin@C_5N_2, carmustine@C_5N_2, and mechlorethamine@C_5N_2 to visualize the non-covalent interactions. The 2D RDG plots and 3D iso surfaces are displayed to visualize the attraction and repulsion between the drug@C_5N_2 complexes. Three color codes were employed to examine the nature of interactions. In the 3D isosurface, the red color reveals the stearic hindrance and the green color represents van der Waals interactions. In contrast, the blue color demonstrates the presence of attractive forces between the drugs and the C_5N_2 substrate such as hydrogen bonding. Besides this, in a 2D plot, red, green, and blue spikes depict stearic repulsions, van der Waals interactions, and hydrogen bonding, respectively (as shown in Figure 3).

The strength of the non-covalent interactions is directly related to the thickness of a particular patch. For instance, a thick patch leads to a stronger interaction as compared to a speckled streak which represents weak interactions between the complexes. Moreover, the electron density (on the x-axis) is directly related to the nature of interactions, i.e., high electron density corresponds to stronger interactions between the complex systems. In 2D plots of cisplatin@C_5N_2, carmustine@C_5N_2, and mechlorethamine@C_5N_2 complexes, the green color spikes manifest the presence of van der Waals interactions ranging from $(0.00 \text{ to } -0.02 \text{ sign}(\lambda_2)\rho(\text{a.u.}))$, showing a significant correlation with the green color 3D isosurface aligned parallelly over pyrazine, benzene, and hydrogenated benzene rings of the C_5N_2 sheet. The red color spikes range from $(0.00 \text{ to } 0.02 \text{ sign}(\lambda_2)\rho(\text{a.u.}))$, manifesting the presence of repulsive interactions between the drugs and the substrate. These spikes show consistency with the red color 3D isosurface between the conjugated rings of the C_5N_2 substrate. The widespread blue color spots in a 2D plot range from $(-0.02 \text{ to } -0.04 \text{ sign}(\lambda_2)\rho(\text{a.u.}))$, representing weak hydrogen bonding between cisplatin@C_5N_2 complex. In contrast, the absence of the blue color spikes in 2D RDG plots of carmustine@C_5N_2 and mechlorethamine@C_5N_2 complexes manifest the lack of hydrogen bonding between the drugs and the surface as displayed with the value ranging from $(-0.02 \text{ to } -0.05 \text{ sign}(\lambda_2)\rho(\text{a.u.}))$ on the x-axis. Moreover, in the case of the carmustine@C_5N_2 complex, the green patches are thicker, showing its greater van der Waals interaction with the C_5N_2 as compared to the cisplatin@C_5N_2, and the mechorethamine@C_5N_2 complexes. However, the cisplatin@C_5N_2 complex exhibits stronger interaction with the substrate due to weak hydrogen bonding. Hence, NCI results revealed significant coherence with the computed results of the interaction energies and

the bond lengths, further validating the presence of non-covalent interactions between the drug@C_5N_2 systems.

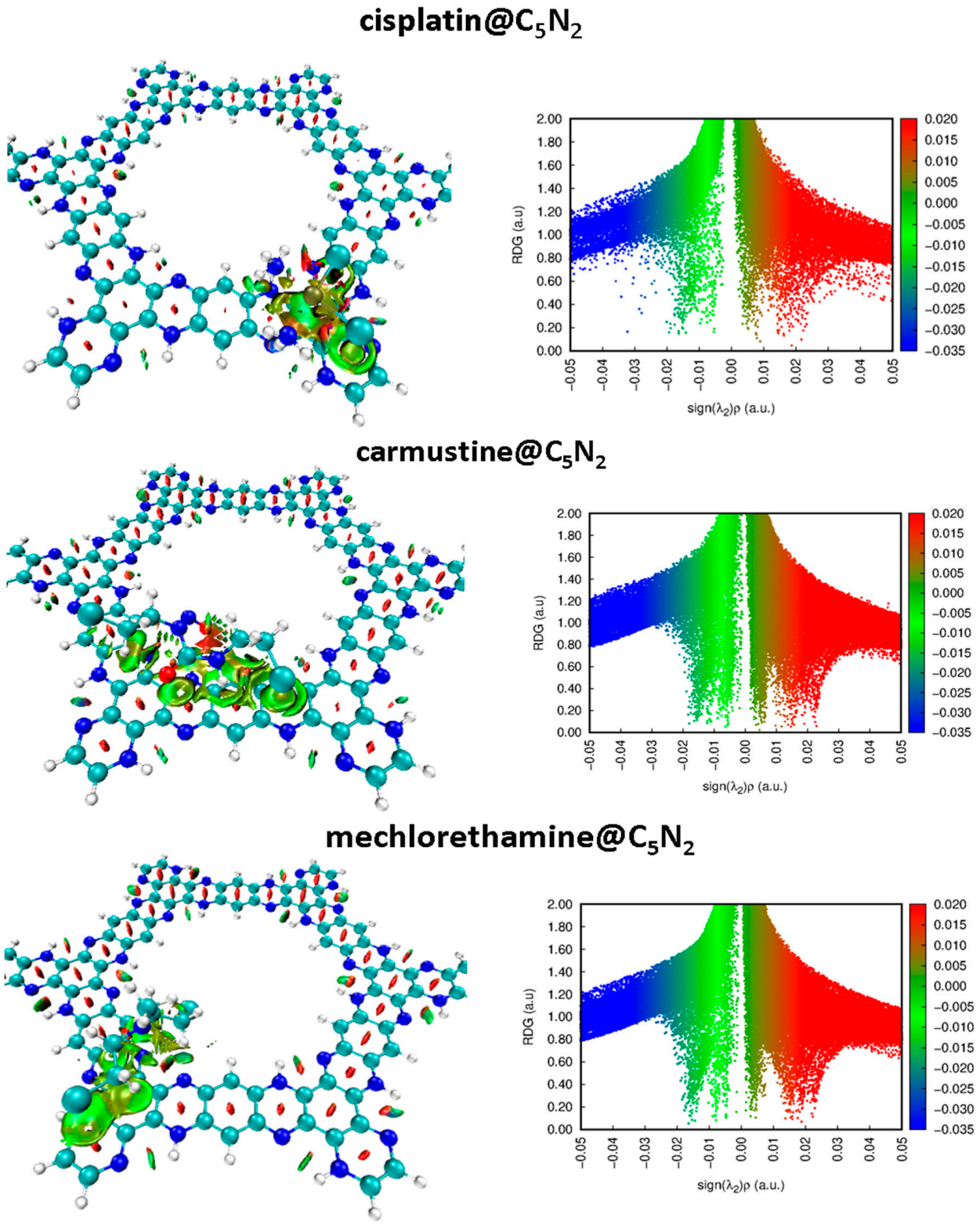


Figure 3. The 3D isosurface and 2D RDG plot highlighting non-covalent interactions between the drugs and the C_5N_2 substrate. The red color highlights regions of stearic hindrance, the green color indicates areas of van der Waals interactions, and the blue color represents hydrogen bonding zones.

3.1.2. Quantum Theory of Atoms in Molecules (QTAIM) Analysis

Quantum theory of atoms in molecules is a primary analyzing tool that provides a comprehensive understanding of the strength and the nature of atomic interactions within the molecular system. It helps in evaluating the presence of covalent and non-covalent bonds at the quantum level. The bonding properties of cisplatin@C_5N_2, carmustine@C_5N_2, and mechlorethamine@C_5N_2 were fundamentally validated through electronic density (ρ) at the bond critical points (BCPs) representing the bonding region between the atoms of the drug and the C_5N_2 sheet. For the cisplatin@C_5N_2 complex, three BCPs were found between H−C, N−H, and Pt−C interacting atoms and two were observed between Cl−C atoms of the complex (as shown in Figure 4). The values of (ρ) range from (0.032 a.u. to 0.0008 a.u.) which reflects the presence of van der Waal interaction between the cisplatin and the C_5N_2 sheet. The highest value of electron density is (0.03 a.u.) between H3 of the cisplatin and N4 of the C_5N_2 sheet manifesting weak hydrogen bonding which substantially correlates with its high interaction energy and decreased bond length. Moreover, the positive values of energy density (H) and Laplacian of electron density $\left(\nabla^2\rho\right)$ range from (0.00008 to 0.0002 a.u.) and (0.02 to 0.08 a.u.), respectively, exhibiting weak interactions between the drug and the substrate. The $-V/G$ ratio is used to estimate the interatomic interactions. It suggests the presence of non-covalent interaction when $-V/G < 1$, and it reveals the formation of a covalent bond if $-V/G > 2$. These values vary from 0.83 a.u. to 0.98 a.u. illustrating non-covalent interactions between the cisplatin@C_5N_2 systems. Also, the values of Lagrangian of kinetic energy (G), and potential energy density (V) indicate non-bonding interactions (as presented in Table 2). In the case of the carmustine@C_5N_2 complex, eight BCPs were located in which three correspond to C−H interactions, two were observed between O−H bonds, and one is identified between O−C, Cl−N, and Cl−C interacted atoms (Figure 4). The values of electron density (ρ) vary from (0.003 a.u.) to (0.01 a.u.) indicating van der Waals interaction. Additionally, the values of the Laplacian of electron density $\left(\nabla^2\rho\right)$, energy density (H,) and $-V/G$ ratio range from (0.018 to 0.041 a.u.), (0.0005 to 0.0012 a.u.), and (0.73 a.u. to 0.87 a.u.), sequentially, manifesting non-covalent interactions between the carmustine@C_5N_2 complexes. Moreover, the values of other parameters including Lagrangian of kinetic energy (G) and potential energy density (V) also illustrate van der Waals interactions (shown in Table 2).

For mechlorethamine, five BCPs were located between the C_5N_2 and the mechlorethamine complex. Among them, four BCPs were found between each of the two atoms (H−N and H−C), while one BCP was observed between Cl1 and C6 interacted atoms (see Figure 4). The values of the electron density (ρ) shift from (0.004–0.01 a.u.), exhibiting non-bonding interactions. Furthermore, the positive values of Laplacian of electron density $\left(\nabla^2\rho\right)$ change from (0.015–0.045 a.u.), illustrating long-range connections between the mechlorethamine@C_5N_2 complex. The values of V/G ratio and energy density (H) among individual atoms ranging from (0.001 to 0.9 a.u.) and (0.0009 to 0.0001), respectively, also manifested weak interactions between the mechlorethamine@C_5N_2 complex. Other topological parameters including (G) and (V) have exhibited van der Waals interaction between the complex as shown in Table 2. These QTAIM parameters revealed consistency in finding the nature and strength of bonding, further manifesting van der Waals interactions between carmustine@C_5N_2 and mechlorethamine@C_5N_2 complexes in combination with weak hydrogen bonding between cisplatin@C_5N_2 complexes. Moreover, these computed results are aligned well and illustrate a significant correlation with the values of interaction energies and NCI analysis.

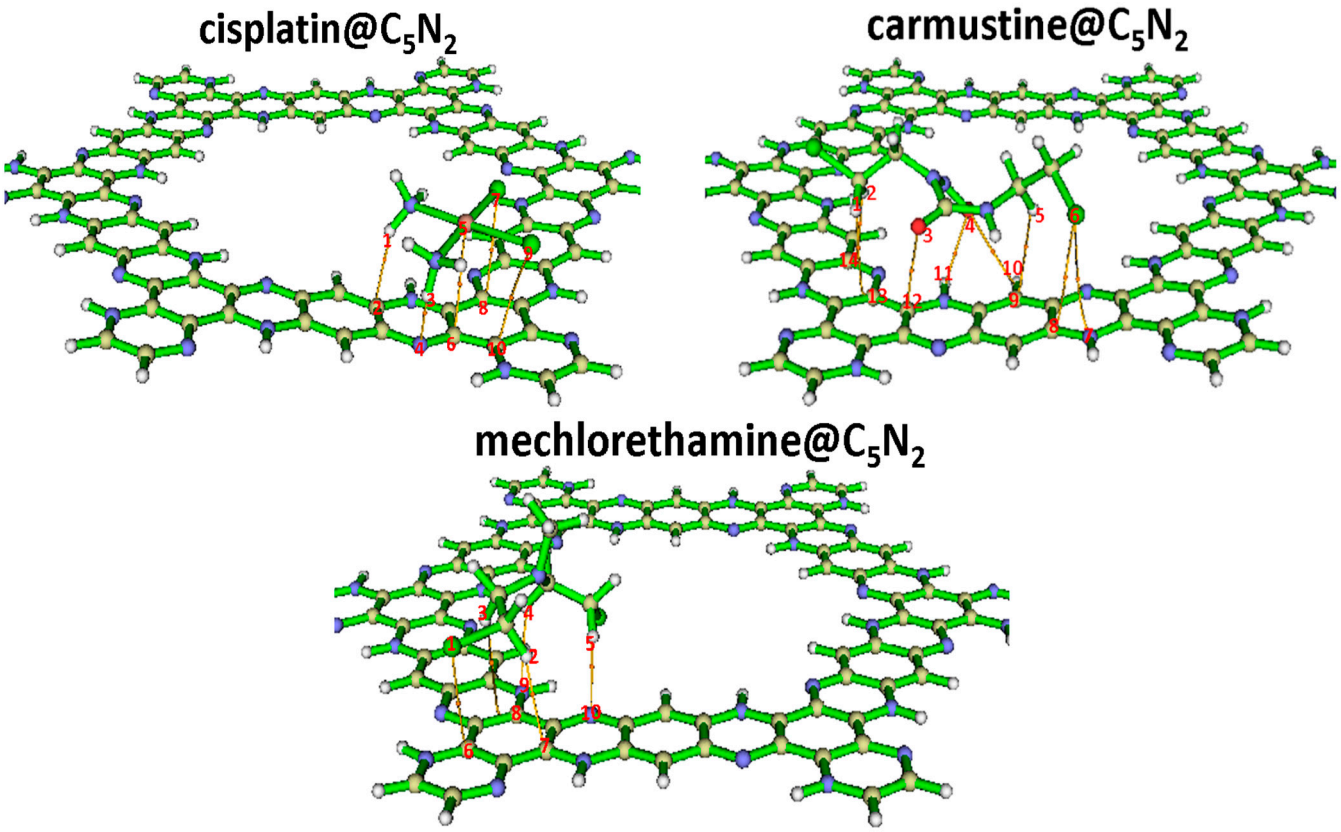


Figure 4. QTAIM analysis of studied drug@C_5N_2 complexes highlighting interacting atoms with corresponding bond critical points (BCPs).

Table 2. QTAIM topological parameters including electron density (ρ), the Laplacian of electron density ($\nabla^2\rho$), the kinetic energy density (G), the potential energy density (V), the total energy density (H), and the $-V/G$ ratio of the cisplatin@C_5N_2, carmustine@C_5N_2, and mechlorethamine@C_5N_2 complexes.

Drugs@C_5N_2	C_5N_2-Drug	ρ (a.u.)	$\nabla^2\rho$ (a.u.)	G (a.u.)	V (a.u.)	H (a.u.)	$-V/G$
cisplatin@C_5N_2	C2−H1	0.0137	0.037	0.008	−0.008	0.0004	0.95
	N4−H3	0.0329	0.087	0.021	−0.021	0.0002	0.98
	C6−Pt5	0.0123	0.034	0.007	−0.007	0.0007	0.90
	C8−Cl7	0.0075	0.022	0.004	−0.004	0.0007	0.83
	C10−Cl9	0.0082	0.025	0.005	−0.004	0.0008	0.85
carmustine@C_5N_2	C13−H1	0.0058	0.018	0.003	−0.002	0.0008	0.75
	C14−H2	0.0030	0.016	0.004	−0.003	0.0006	0.79
	C12−O3	0.0078	0.026	0.005	−0.004	0.0008	0.85
	H11−O4	0.0100	0.041	0.009	−0.008	0.0009	0.89
	H10−O4	0.0050	0.025	0.004	−0.003	0.0012	0.73
	C9−H5	0.0070	0.023	0.004	−0.003	0.0009	0.79
mechlorethamine@C_5N_2	C8−Cl6	0.0063	0.022	0.004	−0.003	0.0008	0.80
	N7−Cl6	0.0064	0.021	0.004	−0.004	0.0005	0.87
	C6−Cl1	0.0081	0.026	0.005	−0.004	0.0009	0.84
	C7−H2	0.0082	0.022	0.005	−0.004	0.0005	0.90
	C8−H3	0.0048	0.015	0.003	−0.002	0.0007	0.77
	N9−H4	0.0091	0.028	0.006	−0.005	0.0005	0.90
	N10−H5	0.0170	0.045	0.011	−0.011	0.0001	0.01

3.1.3. Electron Localization Function (ELF) Analysis

ELF analysis was used to analyze the electron density changes and the nature of interaction after the formation of the complexes. Moreover, it depicts the covalent nature of bonding (indicated by red color) when its value on the y-axis (representing the degree of electron localization) varies between 0.800 and 1.00 (on a color scale). However, it suggests the delocalization of electrons and confirms the presence of non-covalent interactions when the degree of localization ranges from (0.100 to 0.500) as represented by the blue color in ELF plots (Figure 5). For the cisplatin@C_5N_2 complex, the changes in the electron density occurred due to the interaction between the drug and the C_5N_2 sheet (highlighted in Figure 5). The blue color region reflects the presence of non-covalent interaction with a scale range from 0.100 to 0.400 (on the bond axis). It also suggests the shifting of electronic density between the interacting atoms of the complex. In the carmustine@C_5N_2 complex, the electron density changes are reflected clearly after the interaction of the drug and the C_5N_2 sheet. The blue color indicates the area of electron delocalization, further depicting the presence of van der Waals interaction between the complexes. Moreover, the red color scale of the C_5N_2 sheet is shifted from 0.900 (along the bond axis) to the blue color scale (0.200), manifesting the reduction in the localized electrons (covalent nature) after the formation of the mechlorethamine@C_5N_2 complex. These findings indicate the changes and shifting of electron densities and illustrate the presence of non-covalent interactions between the drug@C_5N_2 complexes further correlating with the results of NCI and QTAIM analyses.

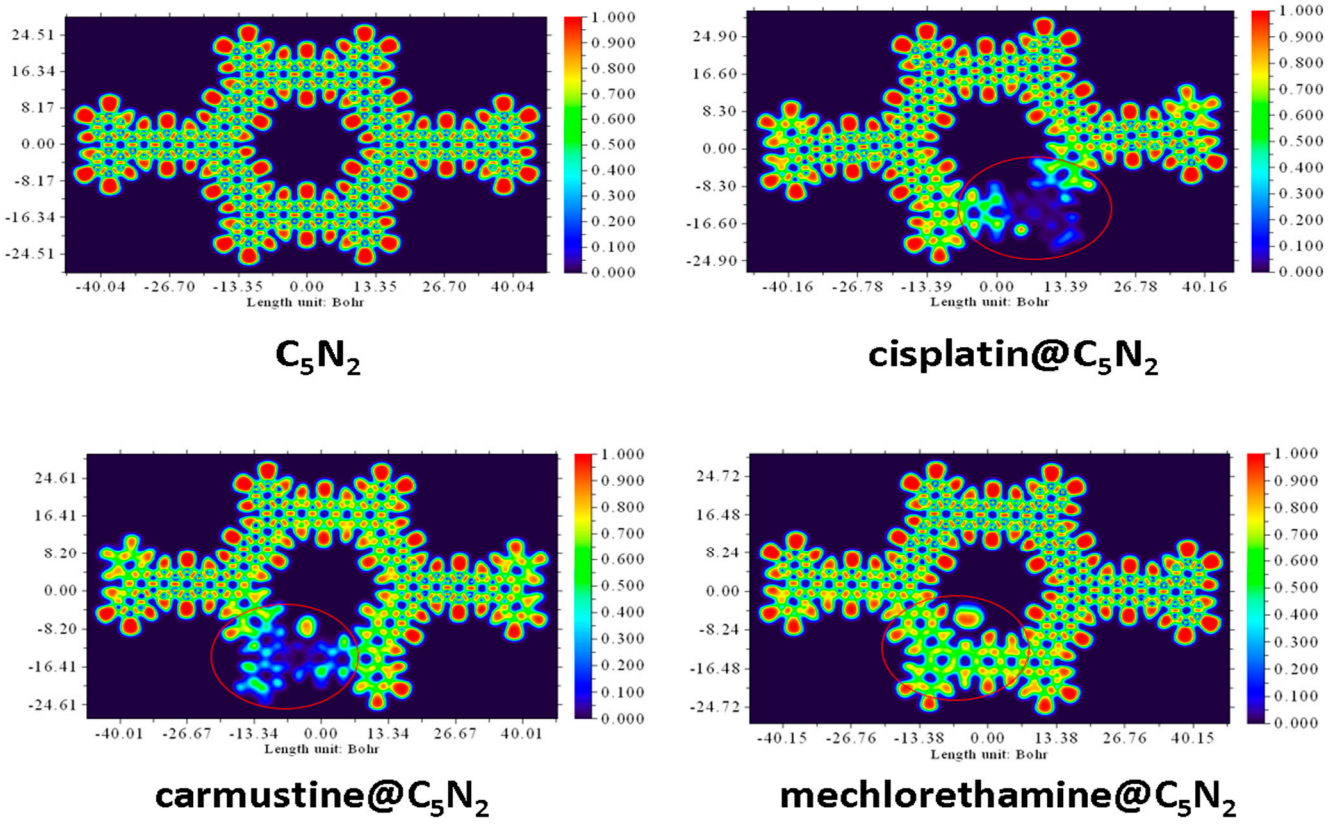


Figure 5. Visual depiction of ELF plots of the bare C_5N_2 sheet and the drug@C_5N_2 complexes. The changes in electron density resulting from the interaction between the drug and the C_5N_2 sheet are highlighted by a red circle.

3.2. Analysis of Electronic Properties

3.2.1. Frontier Molecular Orbital (FMOs) Analysis and Chemical Reactivity Descriptors

Electronic properties of cisplatin@C_5N_2, carmustine@C_5N_2, and mechlorethamine@C_5N_2 complexes were computed to analyze the reactivity of the complexes using the FMO analysis. It is used to identify the active sites of the drugs to check their potential in biological systems. During complex formation, HOMO is responsible for the donation of electronic charges while LUMO corresponds to the acceptance of charges. Furthermore, energies of HOMO−LUMO and spatial distribution of electronic charges were evaluated and visualized for the drug@C_5N_2 complexes through FMO analysis. The high value of HOMO indicates its ability of electron donation, while the high value of LUMO (less negative) illustrates its electron-accepting nature as shown in Table 3. The reactivity and chemical stability of the complexes, i.e., cisplatin@C_5N_2, carmustine@C_5N_2, and mechlorethamine@C_5N_2 were explained by a significant variable, H−L gap (the gap between HOMO and LUMO) represented by (E_g). A small band gap (E_g) reflects high reactivity and polarizability with low kinetic stability of the complexes and vice versa for a large band gap (E_g), i.e., low reactivity and polarizability with high kinetic stability of the complexes. Figure 6 represents the HOMO−LUMO of the C_5N_2 substrate, cisplatin@C_5N_2, carmustine@C_5N_2, and mechlorethamine@C_5N_2 complexes, respectively.

Table 3. Energies of the HOMO and LUMO of the drug@C_5N_2 complexes with their energy gap E_g (eV), and corresponding chemical reactivity descriptors including chemical potential (μ), electrophilicity index (ω), hardness (η), softness (S), and their respective NBO charges.

Complexes	E_{HOMO} (eV)	E_{LUMO} (eV)	E_{gap} (eV)	μ (eV)	ω (eV)	η (eV)	S (eV)	NBO (e^-)
C_5N_2	−3.42	−2.82	0.60	−3.12	16.23	0.30	1.67	–
cisplatin@C_5N_2	−3.41	−2.80	0.57	−3.09	17.68	0.27	1.65	−0.039
carmustine@C_5N_2	−3.41	−2.80	0.57	−3.09	17.68	0.27	1.65	−0.031
mechlorethamine@C_5N_2	−3.39	−2.81	0.58	−3.10	16.51	0.29	1.72	0.479

For the bare C_5N_2 surface, the energy values of the HOMO and LUMO are identified as −3.42 eV and −2.82 eV, respectively, while their E_{H-L} is 0.60 eV. After the formation of the cisplatin@C_5N_2 and carmustine@C_5N_2 complexes, the energy of the HOMO and LUMO has been elevated to −3.41 eV and −2.80 eV, sequentially, with the decrease in the energy gap (0.57 eV). The decrease in the values of the energy gap (E_{H-L}) for cisplatin@C_5N_2 and carmustine@C_5N_2 complexes is directly associated with the increase in energy of HOMO−LUMO (indicating their presence at slightly higher energy levels). Moreover, in the case of the mechlorethamine@C_5N_2 system, the energy gap is reduced to 0.58 eV resulting from the elevation of the energy of HOMO (−3.39 eV) and LUMO (−2.81 eV). However, the decrease in the energy gap of the complexes corresponds to the enhancement of the chemical reactivity of the C_5N_2 substrate (as compared to the pristine C_5N_2 sheet) as shown in Table 3.

Among these complexes, the energy of HOMO of mechlorethamine@C_5N_2 complex (−3.39 eV) indicates its tendency of electron donation as it is shifted on a higher energy level, while the energy of LUMO of cisplatin and carmustine (−2.80 eV) reflects its ability of electron acceptance within the complex. The reduction in the energy gap manifests a feasible interaction owing to an effective charge transfer between the drugs and the C_5N_2 sheet, resulting in a stabilized complex. The orbital spatial distribution of the cisplatin@C_5N_2, carmustine@C_5N_2, and mechlorethamine@C_5N_2 complexes is represented in Figure 6. In the case of cisplatin@C_5N_2 and carmustine@C_5N_2 complexes, the isosurface of the HOMO is completely distributed over the C_5N_2 surface while LUMO is spread slightly over their re-

spective drugs. In contrast, in the mechlorethamine@C_5N_2 complex, the HOMO isosurface is widely distributed over the mechlorethamine drug and the substrate while the LUMO is entirely dispersed over the surface of the C_5N_2 sheet. These electron cloud patterns reflect electron density shifts between the drugs and the C_5N_2 carrier after complex formation and exhibit a major correlation with the findings of the interaction energy and the topology analyses. The reactivity and stability of the drugs, the C_5N_2 substrate, and the drugs@C_5N_2 complexes are explained by the computed values of the chemical reactivity descriptors. The more negative value of (μ) in the mechlorethamine@C_5N_2 complex (−3.10 eV) indicates its least reactivity and higher stability as compared to the cisplatin@C_5N_2 and carmustine@C_5N_2 complexes with relatively less negative (μ) value (−3.09 eV). Moreover, a lower value of (ω) in the mechlorethamine@C_5N_2 complex (16.51 eV) manifests its nucleophilic nature towards the C_5N_2 sheet while a high (ω) value in the cisplatin@C_5N_2 and carmustine@C_5N_2 complexes (17.68 eV) indicate their electrophilic nature towards the C_5N_2 substrate. Between the drug@C_5N_2 complexes, the highest hardness value is (0.29 eV) in the mechlorethamine@C_5N_2 complex, manifesting its less polarizability and a harder nature having a large energy gap as compared to the cisplatin@C_5N_2 and carmustine@C_5N_2 complexes as presented in Table 3. These findings demonstrate a better interaction of the drugs with the C_5N_2 sheet and illustrate enhanced stability in (mechlorethamine@C_5N_2 complex) and higher reactivity in cisplatin@C_5N_2 and carmustine@C_5N_2 complexes.

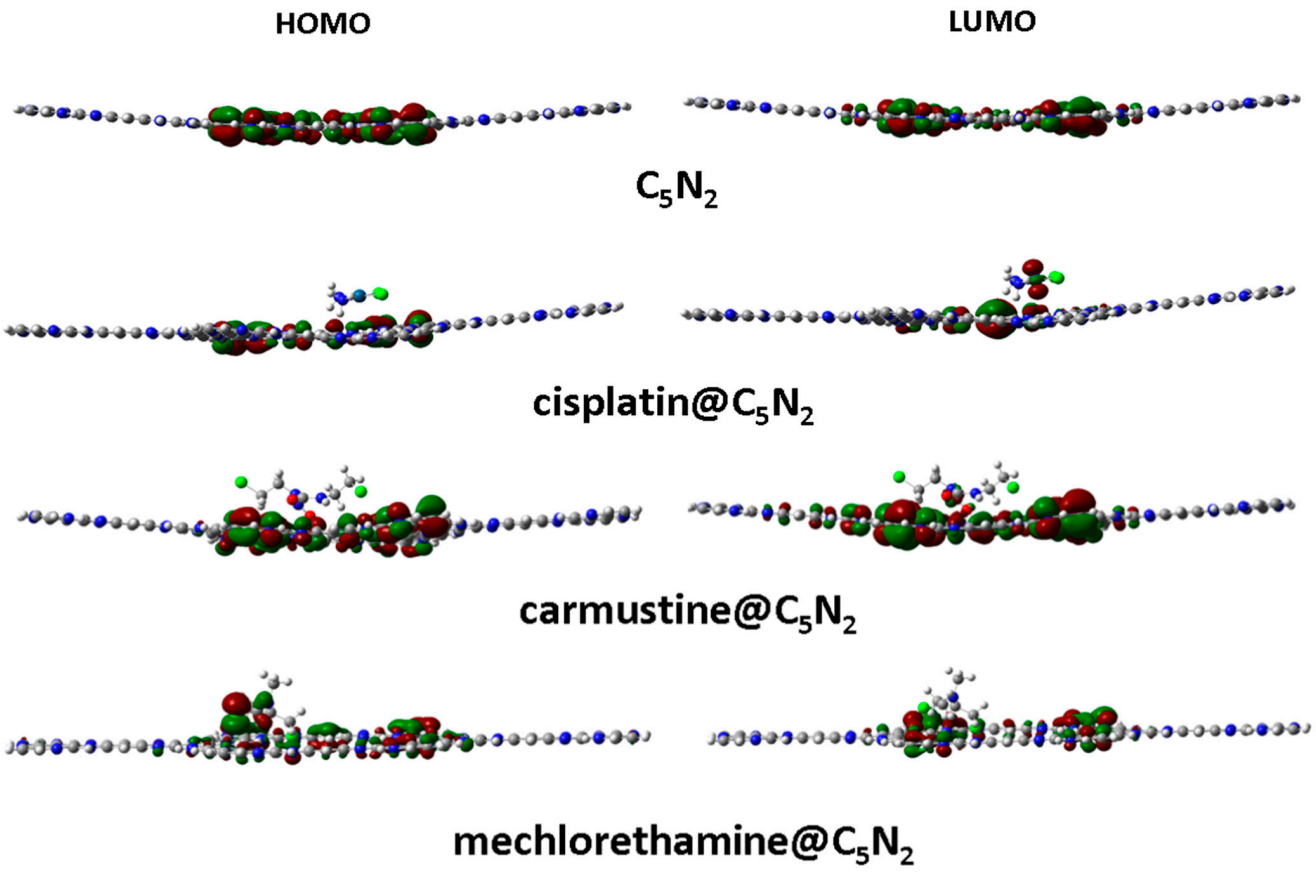


Figure 6. Spatial distribution of the HOMO−LUMO of the bare C_5N_2 sheet along with the drug@C_5N_2 complexes.

3.2.2. Density of States (DOS) Analysis

The electronic structure of the complexes, i.e., cisplatin@C_5N_2, carmustine@C_5N_2, and mechlorethamine@C_5N_2 were evaluated through the DOS analysis to visualize the energy levels and their relative positions. The contributions of the HOMO−LUMO and the E_{H-L}

gap within the complexes were also verified through the DOS plots as shown in Figure 7. The DOS spectra of the cisplatin@C_5N_2, carmustine@C_5N_2, and mechlorethamine@C_5N_2 complexes manifest a slight shift in the HOMO−LUMO peaks as compared to the peaks of the pristine C_5N_2 sheet (−3.42 eV and −2.82 eV, respectively). The HOMO of the cisplatin@C_5N_2, carmustine@C_5N_2, and mechlorethamine@C_5N_2 complexes is shifted to a less negative position (−3.41 eV and −3.39 eV) while LUMO emerged at (−2.80 eV and −2.81 eV) suggesting enhanced chemical reactivity and a charge transfer between the interacting atoms of the complexes. The peak intensities reflect the contribution of the orbitals and the availability of the electronic states at a specific energy level. Hence, the shifting of the peaks and the enhancement of the orbitals of HOMO−LUMO result in the reduction in the energy gap which further reinforces the findings of the FMO analysis.

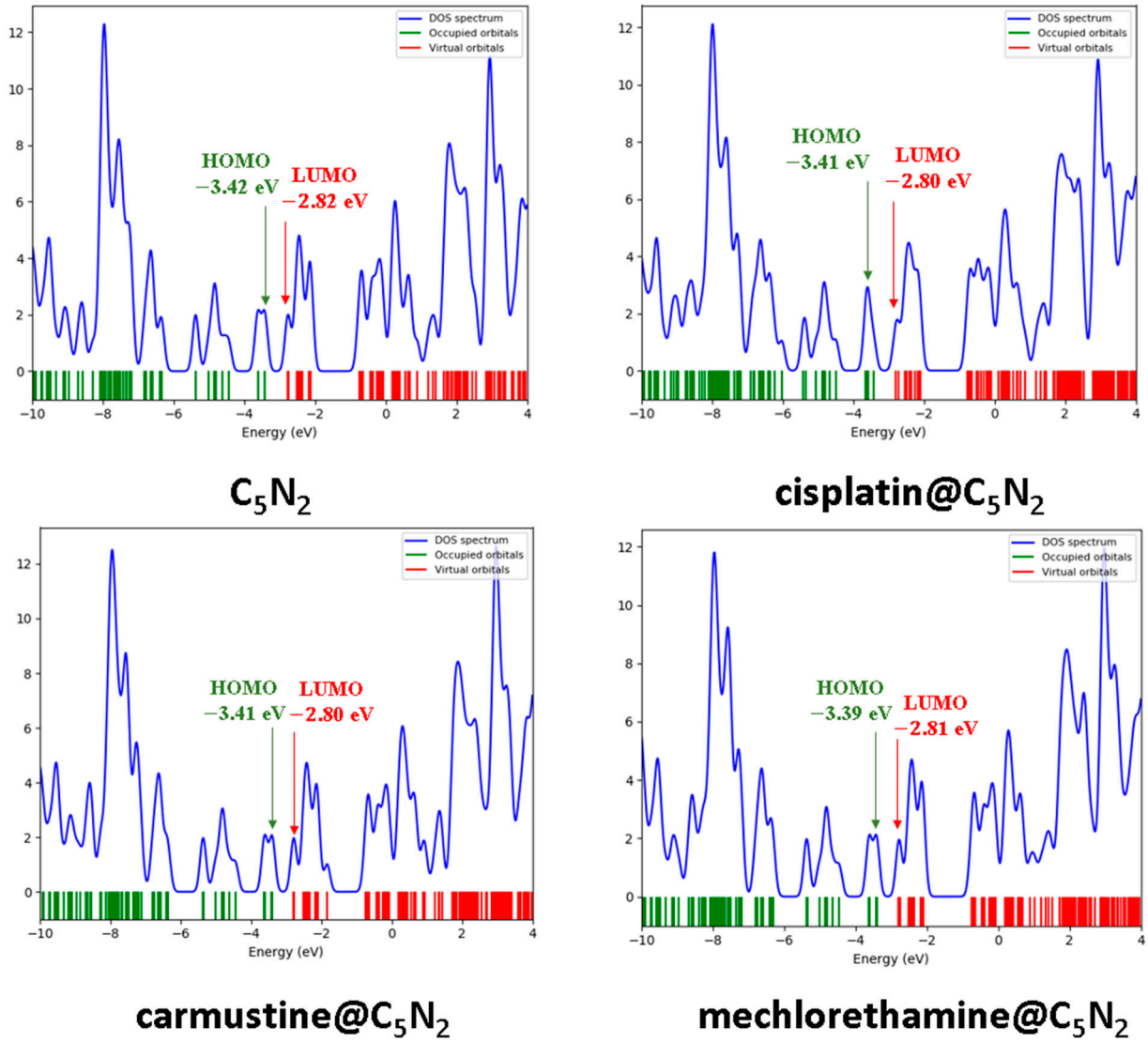


Figure 7. Graphical illustration of DOS spectra highlighting the HOMO−LUMO energy gap of the bare C_5N_2 sheet and drug@C_5N_2 complexes.

3.2.3. NBO and EDD Analyses

Natural bond orbital analysis plays a significant role in illustrating the transfer of charges between the drug@C_5N_2 complexes. After the formation of the cisplatin@C_5N_2 complex, the value of NBO charge on the cisplatin drug is increased to $-0.039\ e^-$ which shows the electronic density is shifted from the C_5N_2 sheet to the cisplatin drug. The

negative charge of nitrogen and chlorine atoms bonded with H1, H3, and Pt5 has also been elevated to $-0.98\ e^-$, $-0.99\ e^-$, and $-0.39\ e^-$ in sequence from $-0.20\ e^-$ and $-0.33\ e^-$ after complex formation. Moreover, the charge on H1, H3, and Pt5 atoms of the cisplatin drug has also been increased from $0.180\ e^-$, $0.169\ e^-$, and $0.04\ e^-$ to $0.419\ e^-$, $0.430\ e^-$, and $0.24\ e^-$, respectively, after the interaction with C2, N4, and C6 making H1, H3, and Pt5 atoms of the drug electron deficient. However, the amount of charge attracted from the sheet is greater than the charge donated by the drug, manifesting that the major electron density is shifted from the C_5N_2 sheet to the cisplatin drug after interaction. In the carmustine@C_5N_2 complex, the negative value of the NBO charge ($-0.031\ e^-$) illustrates the transfer of electronic density from the C_5N_2 sheet to the carmustine drug. The oxygen atoms of the carmustine attract electrons towards themselves making the C_5N_2 sheet electron deficient. The negative charges on O3 and O4 of the carmustine have been increased from $-0.24\ e^-$ and $-0.25\ e^-$ to $-0.62\ e^-$ and $-0.39\ e^-$, respectively, after complexation with C12, H10, and H11 of the C_5N_2 substrate. The value of negative charge on the nitrogen of carmustine has also been elevated from $-0.32\ e^-$ to $-0.34\ e^-$. Moreover, the positive values of the electronic charges in the alkyl chain of carmustine intensified up to $-0.40\ e^-$, $-0.24\ e^-$, $-0.25\ e^-$, and $-0.38\ e^-$ after complex formation. These clear escalations in the charge values of cisplatin and carmustine manifests their electron-accepting nature while presenting C_5N_2 as a donor substrate in the cisplatin@C_5N_2 and carmustine@C_5N_2 complexes. In contrast, the positive value of electronic charge ($0.479\ e^-$) over mechlorethamine indicates the transfer of charge from the drug to the C_5N_2 sheet. The nitrogen (N10) attracts electron density from the H5 atom of the mechlorethamine and its charge value is increased from $-0.51\ e^-$ to $-0.56\ e^-$ in a complex. The charge on Cl1 is decreased from $-0.21\ e^-$ to $-0.10\ e^-$ after interacting with C6 of the C_5N_2 sheet. These findings show that the charge had been transferred from the mechlorethamine drug to the C_5N_2 sheet in a complex system. Hence in the cisplatin@C_5N_2 complex, the highest amount of charge, i.e., ($0.039\ e^-$) is shifted from the C_5N_2 surface to the drug molecule, while in mechlorethamine@C_5N_2, $0.479\ e^-$ of charge is captivated from the drug molecule to the pyrazine and benzene rings of the C_5N_2 substrate after association as shown in Table 3.

To validate and comprehend the NBO results, EDD was performed to elucidate the electron density shifts between the drug and the C_5N_2 sheet in the drug@C_5N_2 complexes. Two color codes were used to analyze the charge accumulation and depletion, i.e., red and blue, sequentially, after the association of the drug and the C_5N_2 carrier. The EDD results were computed by subtracting the sum of the individual electron densities of drugs and the C_5N_2 sheet from the electron density of drug@C_5N_2 complexes as represented by $\Delta\rho$ where

$$\Delta\rho = \rho_{\text{drug@C}_5\text{N}_2} - \left(\rho_{\text{C}_5\text{N}_2} + \rho_{\text{drug}}\right) \tag{9}$$

The negative values of $\Delta\rho$ are represented by red (charge accumulation) while the positive value of $\Delta\rho$ is indicated by blue color (charge depletion) as represented by EDD portrayals in Figure 8. For the cisplatin@C_5N_2 complex, the electron density is shifted from the benzene ring of the C_5N_2 carrier (as represented by the blue color isosurface) to the electronegative chlorine and nitrogen atoms of the drug (depicted by the red color isosurface over the drug molecule). Moreover, the nitrogen and carbon atoms of the pyrazine ring of the C_5N_2 sheet accepted electron density (depicted by the red isosurface) from the hydrogen atoms of the cisplatin (illustrated by the blue color isosurface over H1 and H3 atoms) after interaction as shown in Figure 8. In the carmustine@C_5N_2 complex, the electron density is shifted from the conjugated pyrazine and benzene rings of the C_5N_2 surface (as illustrated by the blue color isosurface) to the electronegative atoms of the drug (indicated by the red color) after their interaction within a complex. The red color isosurface is also distributed over the edged aromatic pyrazine ring of the C_5N_2 sheet because it exhibits the least

interaction with the drug molecule. In the mechlorethamine@C_5N_2 complex, the blue color isosurface of the drug (mainly on H atoms) represents electron deficiency after interaction with the substrate atoms. Moreover, the red isosurface over pyrazine and benzene rings of the substrate depicts the withdrawal of electron density from the drug (H5 and C7) to the C_5N_2 sheet after complex formation as indicated by Figure 8. Consequently, the isosurface and findings of EDD correlate significantly with the results of FMO and NBO analyses.

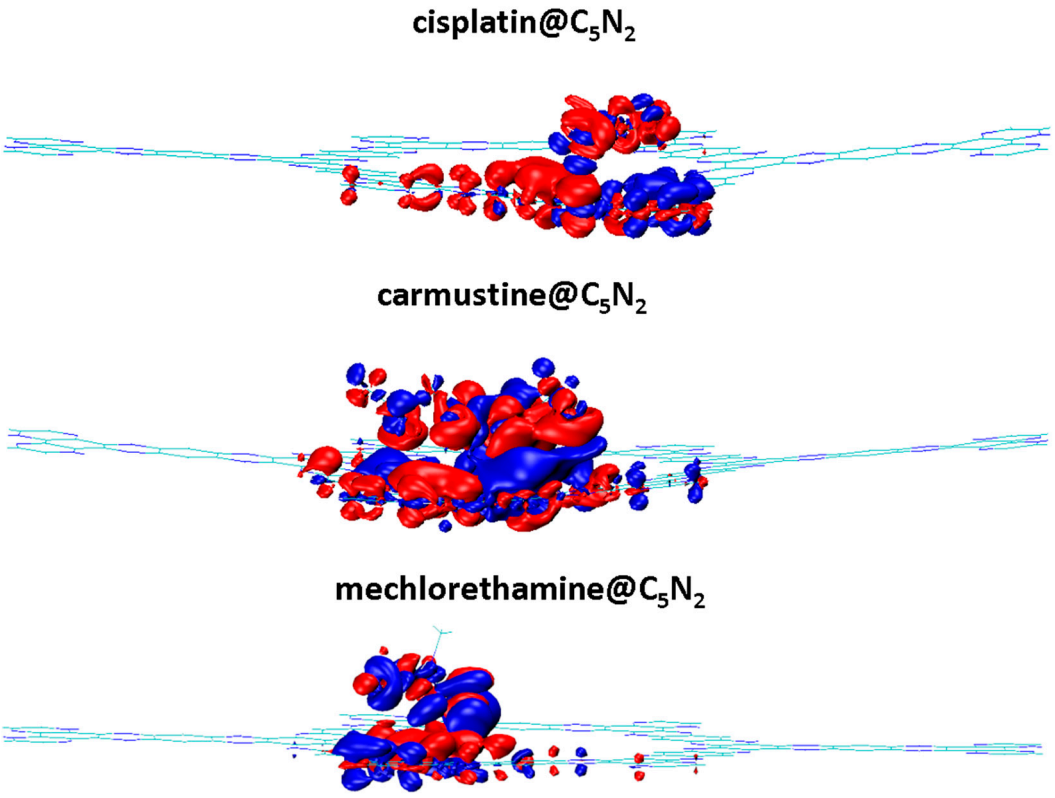


Figure 8. The portrayal of the electron density distribution of cisplatin@C_5N_2, carmustine@C_5N_2, and mechlorethamine@C_5N_2 complexes. The red color represents the electron density accumulated region while the blue color is related to the electron density depleted region.

4. Recovery Time

The desorption of the anticancer drugs plays a crucial part in targeted drug delivery which was evaluated by analyzing the recovery times of the drugs. The theoretical calculation of the recovery time (τ) [133] for the desorption of cisplatin, carmustine, and mechlorethamine from the surface of the C_5N_2 sheet was performed using the expression

$$\tau = v^{-1} e^{\left(\frac{-E_{ads}}{KT}\right)} \quad (10)$$

Here, T is the temperature, v is the attempt frequency ($v = 10^{16}$ s^{-1}) [134] and K is the Boltzmann's constant (~1.99×10^{-3} kcal mol^{-1} K^{-1}). At 473 K, the recovery time of the cisplatin@C_5N_2 and the carmustine@C_5N_2 complexes is 5.43×10^{-4} s and 1.22×10^{-7} s, respectively. Moreover, for the mechlorethamine@C_5N_2 complex, the recovery time is 1.52×10^{-8} s. These findings manifest that mechlorethamine and carmustine will desorb faster having shorter recovery times, while cisplatin will desorb slowly following the order, i.e., cisplatin@C_5N_2 < carmustine@C_5N_2 < mechlorethamine@C_5N_2, further correlating with the results of interaction energies. Moreover, the recovery time of the drugs is exponentially decreased with the increase in the temperature as shown in Table S2. These exponential temperature-dependent trends demonstrate how thermal energy can modulate

drug release rates, suggesting potential for hyperthermia-triggered delivery in therapeutic applications [135].

5. Solvent Effect

To gain insight into the interaction and stability of the drug@C_5N_2 complexes in a realistic media, SMD (solvation model based on density) is employed at the same level of theory [136]. This model provides a precise illustration of both the electrostatic and non-electrostatic interactions of the system and is parameterized for a wider range of solvents [137,138]. Moreover, it can calculate the solvation energies that are crucial for bonding and interaction strengths of large and complex geometries with different solvents [139,140]. It has also been used to evaluate the hydration-free energies in drug design [141]. Since water is a key component of the human biochemical system, it was used as a solvent in this study. The influence of the solvent on interactions between the drug molecules and the C_5N_2 substrate was investigated using the expression [142]

$$\Delta E_{solvation} = E_{sol} - E_{gas} \quad (11)$$

ΔE corresponds to the solvation energy of the complex, where the total energy of the complexes, i.e., drugs@C_5N_2 in solvent and gas phases is represented by E_{sol} and E_{gas}, respectively. The solvation energy of the cisplatin@C_5N_2, and carmustine@C_5N_2 complexes is increased to -65.13 kcal mol^{-1} and -51.11 kcal mol^{-1}, respectively, which confirms their stability in the aqueous phase. Additionally, for the mechlorethamine@C_5N_2 complex, the solvation energy is increased to -46.82 kcal mol^{-1}, manifesting its significant adsorption in water media. These negative values revealed stable interaction of the drugs with the C_5N_2 substrate in the solvent phase. The dipole moment is another parameter that is used to investigate the solubility and polarity of a complex in an aqueous phase. The calculated value of a dipole moment for the C_5N_2 substrate, cisplatin@C_5N_2, carmustine@C_5N_2, and mechlorethamine@C_5N_2 are observed as 0.02 D, 6.10 D, 2.69 D, and 1.83 D in gaseous and 0.30 D, 7.43 D, 5.33 D, and 2.43 D in solvent phases, respectively. Compared to the C_5N_2 sheet, the high dipole moment of the complexes indicates better solubility, localization, and directional interaction in polar solvents. This manifests that the hydrophilicity of the cisplatin@C_5N_2, carmustine@C_5N_2, and mechlorethamine@C_5N_2 complexes also increases after complexation, which facilitates easy circulation of the drugs within the biological systems. The values of the solvation energy of cisplatin@C_5N_2, carmustine@C_5N_2, and mechlorethamine@C_5N_2 complexes with their respective dipole moments in gaseous and solvent phases are presented in Table S3. The solvation energy analysis combined with dipole moment shifts reveals how aqueous environments promote drug release through competitive hydrogen bonding and electrostatic screening [143]. Notably, pH-dependent studies manifest that solvation effect is significantly enhanced in acidic conditions, where protonation of substrates nitrogen sites reduces drug coordination strength compared to physiological pH, which is further advantageous for targeted drug delivery [144].

By aligning these theoretical insights with experimental designs, this study provides clear insight toward biomedical applications of C_5N_2 in targeted cancer therapy. The observed favorable interaction energies, solvation characteristics, and fast recovery times suggest that C_5N_2 can effectively load and release cisplatin, carmustine, and mechlorethamine under physiological conditions. These findings point toward its promising use in targeted chemotherapy, where site-specific drug release is critical to minimizing side effects. Future experimental validation, including in vitro cytotoxicity tests and in vivo pharmacokinetic studies [145], would be useful to validate theoretical results into clinical practice. Moreover, tunable surface properties of C_5N_2 offer opportunities for functionalization with targeting ligands [146], which enable its precise delivery to specified cancer cells. Our computed

interaction trends are also consistent with reported experimental and theoretical findings, further supporting the validity of this approach [147].

6. Conclusions

Computational studies were performed to analyze the interaction behavior of anticancer drugs including cisplatin, carmustine, and mechlorethamine over the surface of the C_5N_2 sheet using DFT calculations. Geometry optimization of the drugs, C_5N_2 sheet, and their complexes (cisplatin@C_5N_2, carmustine@C_5N_2, and mechlorethamine@C_5N_2) was performed at the PBE0-D3BJ/def2SVP level of theory. Different positions of the drugs over the substrate were validated and the most suitable configuration was used to analyze the nature of interaction between the complexes. The highest interaction energy was obtained for cisplatin@C_5N_2 (-27.60 kcal mol^{-1}) following carmustine@C_5N_2 (-19.69 kcal mol^{-1}) and mechlorethamine@C_5N_2 (-17.79 kcal mol^{-1}) complexes. Topology analysis of the complexes was performed to analyze the strength and the type of bonding between the drug@C_5N_2 systems. The QTAIM and NCI analyses of the complexes manifested the presence of non-covalent interactions between the drug and the C_5N_2 sheet. In the case of carmustine@C_5N_2 and mechlorethamine@C_5N_2 complexes, van der Waals interactions were observed as green color isosurface and patches in 3D and 2D RDG plots. Conversely, weak hydrogen bonding has also been observed in the cisplatin@C_5N_2 complex as depicted by the blue color spots in a 2D NCI plot. The higher values of electron density (ρ) and Laplacian of electron density ($\nabla^2\rho$) manifested non-covalent interactions correlating with the NCI results. ELF analysis was carried out to estimate the degree of electron delocalization between the complexes. Reactivity and interaction of the complexes were enhanced with the reduction in the HOMO$-$LUMO gap (E_g). The chemical potential and electrophilicity index of the cisplatin@C_5N_2 and carmustine@C_5N_2 complexes indicate their higher reactivity while mechlorethamine@C_5N_2 is the least reactive among them. DOS analysis exhibited a significant correlation with the findings of the FMO analysis, further confirming the decrease in the energy gap due to the shifting of the peaks and the enhancement of the orbitals. Electron density shifts were computed and analyzed through NBO analysis and EDD portrayals. Recovery time was calculated to analyze the desorption behavior of the drugs from the C_5N_2 surface. The mechlorethamine drug recovered faster while carmustine and cisplatin drugs manifested slow recovery from the surface of the C_5N_2 sheet, exhibiting a substantial correlation with the results of the interaction energy. SMD solvation model was employed to evaluate the solvation energy of the complexes and the calculations were performed at the same level of theory by employing water as a solvent. The interaction of the complexes was enhanced in solvent media. The higher values of the dipole moment indicate better solubility, localization, and directional interaction of the complexes in a solvent phase. Moreover, the observed interaction energies, solvation behavior, and electronic properties support the stability and bioavailability of the drug@C_5N_2 complexes. These findings lay the groundwork for future experimental validation, including drug loading capacity measurements, controlled drug release kinetics, surface functionalization strategies and in vitro–in vivo biocompatibility studies of C_5N_2-based substrates. Further experimental work will be essential to translate these computational insights into practical biomedical applications.

Supplementary Materials: The following supporting information is available online: https://www.mdpi.com/article/10.3390/chemistry7030098/s1. Figures S1–S3: Optimized geometries of the cisplatin@C_5N_2, carmustine@C_5N_2 and mechlorethamine@C_5N_2 complexes with different orientations of the drugs over the C_5N_2 sheet; Tables S1–S3: Interaction energies (kcal mol^{-1}), recovery time (τ) at different temperatures, solvation energies (kcal mol^{-1}, and dipole moment (D) in gas and solvent media of the drug@C_5N_2 complexes.

Author Contributions: Validation, analysis, investigation, data curation, writing—original draft preparation, writing—review and editing, visualization, S.H.M.Z.; conceptualization, methodology, computational resources, supervision, M.A.H.; validation, computational resources, A.L.; writing—review and editing, M.A., M.A.H. and A.L. All authors have read and agreed to the published version of the manuscript.

Funding: This research received no external funding.

Institutional Review Board Statement: Not applicable.

Informed Consent Statement: Not applicable.

Data Availability Statement: Data is contained within the article and Supplementary File.

Conflicts of Interest: The authors declare no conflicts of interest.

References

1. Siegel, R.L.; Miller, K.D.; Wagle, N.S.; Jemal, A. Cancer statistics, 2023. *CA A Cancer J. Clin.* **2023**, *73*, 17–48. [CrossRef] [PubMed]
2. Siegel, R.L.; Wagle, N.S.; Cercek, A.; Smith, R.A.; Jemal, A. Colorectal cancer statistics, 2023. *CA A Cancer J. Clin.* **2023**, *73*, 233–254. [CrossRef]
3. Cao, S.; Wei, Y.; Huang, J.; Yue, Y.; Deng, A.; Zeng, H.; Wei, W. A bibliometric worldview of breast-conserving surgery for breast cancer from 2013 to 2023. *Front. Oncol.* **2024**, *14*, 1405351. [CrossRef]
4. Srinivasan, D.; Subbarayan, R.; Srivastava, N.; Radhakrishnan, A.; Adtani, P.N.; Chauhan, A.; Krishnamoorthy, L. A comprehensive overview of radiation therapy impacts of various cancer treatments and pivotal role in the immune system. *Cell Biochem. Funct.* **2024**, *42*, e4103. [CrossRef] [PubMed]
5. Sharma, A.; Jasrotia, S.; Kumar, A. Effects of chemotherapy on the immune system: Implications for cancer treatment and patient outcomes. *Naunyn-Schmiedeberg's Arch. Pharmacol.* **2024**, *397*, 2551–2566. [CrossRef] [PubMed]
6. Liu, B.; Zhou, H.; Tan, L.; Siu, K.T.H.; Guan, X.-Y. Exploring treatment options in cancer: Tumor treatment strategies. *Signal Transduct. Target. Ther.* **2024**, *9*, 175. [CrossRef] [PubMed]
7. Kar, A.; Agarwal, D.G.; Agarwal, D.S. A Review On Nanostructure Drug Carriers for Treatment and Management of Neuroendocrine Cancer. *Int. J. Pharm. Sci.* **2023**, *14*, 1–9. [CrossRef]
8. Anand, U.; Dey, A.; Chandel, A.K.S.; Sanyal, R.; Mishra, A.; Pandey, D.K.; De Falco, V.; Upadhyay, A.; Kandimalla, R.; Chaudhary, A. Cancer chemotherapy and beyond: Current status, drug candidates, associated risks and progress in targeted therapeutics. *Genes Dis.* **2023**, *10*, 1367–1401. [CrossRef]
9. Romani, A.M. Cisplatin in cancer treatment. *Biochem. Pharmacol.* **2022**, *206*, 115323. [CrossRef]
10. Strojan, P.; Vermorken, J.B.; Beitler, J.J.; Saba, N.F.; Haigent, M., Jr.; Bossi, P.; Worden, F.P.; Langendijk, J.A.; Eisbruch, A.; Mendenhall, W.M. Cumulative cisplatin dose in concurrent chemoradiotherapy for head and neck cancer: A systematic review. *Head Neck* **2016**, *38*, E2151–E2158. [CrossRef]
11. Song, M.; Cui, M.; Liu, K. Therapeutic strategies to overcome cisplatin resistance in ovarian cancer. *Eur. J. Med. Chem.* **2022**, *232*, 114205. [CrossRef] [PubMed]
12. Li, F.; Zheng, Z.; Chen, W.; Li, D.; Zhang, H.; Zhu, Y.; Mo, Q.; Zhao, X.; Fan, Q.; Deng, F. Regulation of cisplatin resistance in bladder cancer by epigenetic mechanisms. *Drug Resist. Updates* **2023**, *68*, 100938. [CrossRef] [PubMed]
13. Sala, L.; Perecko, T.; Mestek, O.; Pinkas, D.; Homola, T.; Kocisek, J. Cisplatin-cross-linked DNA origami nanostructures for drug delivery applications. *ACS Appl. Nano Mater.* **2022**, *5*, 13267–13275. [CrossRef]
14. Lemjabbar-Alaoui, H.; Hassan, O.U.; Yang, Y.-W.; Buchanan, P. Lung cancer: Biology and treatment options. *Biochim. Biophys. Acta (BBA)-Rev. Cancer* **2015**, *1856*, 189–210. [CrossRef] [PubMed]
15. Shirbin, S.J.; Ladewig, K.; Fu, Q.; Klimak, M.; Zhang, X.; Duan, W.; Qiao, G.G. Cisplatin-induced formation of biocompatible and biodegradable polypeptide-based vesicles for targeted anticancer drug delivery. *Biomacromolecules* **2015**, *16*, 2463–2474. [CrossRef]
16. Wagstaff, A.J.; Brown, S.D.; Holden, M.R.; Craig, G.E.; Plumb, J.A.; Brown, R.E.; Schreiter, N.; Chrzanowski, W.; Wheate, N.J. Cisplatin drug delivery using gold-coated iron oxide nanoparticles for enhanced tumour targeting with external magnetic fields. *Inorganica Chim. Acta* **2012**, *393*, 328–333. [CrossRef]
17. Perveen, M.; Nazir, S.; Arshad, A.W.; Khan, M.I.; Shamim, M.; Ayub, K.; Khan, M.A.; Iqbal, J. Therapeutic potential of graphitic carbon nitride as a drug delivery system for cisplatin (anticancer drug): A DFT approach. *Biophys. Chem.* **2020**, *267*, 106461. [CrossRef]
18. Weiss, R.B.; Issell, B.F. The nitrosoureas: Carmustine (BCNU) and lomustine (CCNU). *Cancer Treat. Rev.* **1982**, *9*, 313–330. [CrossRef] [PubMed]

19. Khanizadeh, A.; Ghaemi, A.; Pourmadadi, M.; Javadi, S.; Rahdar, A.; Yazdian, F.; Ghazy, E.; Pandey, S. Advancing cancer therapy: Unveiling the cutting-edge potential of carmustine nano carriers for targeted treatment. *J. Drug Deliv. Sci. Technol.* **2024**, *99*, 105943. [CrossRef]
20. Ahmad, S.; Khan, I.; Pandit, J.; Emad, N.A.; Bano, S.; Dar, K.I.; Rizvi, M.M.A.; Ansari, M.D.; Aqil, M.; Sultana, Y. Brain targeted delivery of carmustine using chitosan coated nanoparticles via nasal route for glioblastoma treatment. *Int. J. Biol. Macromol.* **2022**, *221*, 435–445. [CrossRef]
21. Chen, S.; Qiu, Q.; Wang, D.; She, D.; Yin, B.; Chai, M.; He, H.; Heo, D.N.; Wang, J. Long acting carmustine loaded natural extracellular matrix hydrogel for inhibition of glioblastoma recurrence after tumor resection. *Front. Chem. Sci. Eng.* **2022**, *16*, 536–545. [CrossRef]
22. Bayat, M.; Taherpour, A.A.; Elahi, S.M.; Fellowes, T. Separation of anticancer medicines carmustine, lomustine, semustine and melphalan by PAMAM dendrimer: A theoretical study. *J. Iran. Chem. Soc.* **2018**, *15*, 1223–1234. [CrossRef]
23. Kamel, M.; Mohammadi, M.; Mohammadifard, K.; Mahmood, E.A.; Heravi, M.R.P.; JM, A.H.; Hossaini, Z. Comprehensive theoretical prediction of the stability and electronic properties of hydroxyurea and carmustine drugs on pristine and Chitosan-functionalized graphitic carbon nitride in vacuum and aqueous environment. *Vacuum* **2023**, *207*, 111565. [CrossRef]
24. Rani, V.; Venkatesan, J.; Prabhu, A. Carmustine-Loaded Liposomal Delivery Effectively Targets Malignant Glioma Cells and Seizes Endothelial Sprouting In vitro. *J. Clust. Sci.* **2024**, *35*, 1211–1221. [CrossRef]
25. Mortazavifar, A.; Raissi, H.; Akbari, A. DFT and MD investigations on the functionalized boron nitride nanotube as an effective drug delivery carrier for Carmustine anticancer drug. *J. Mol. Liq.* **2019**, *276*, 577–587. [CrossRef]
26. Solomon, J.; Jacobs, E.M.; Bateman, J.R.; Lukes, R.J.; Weiner, J.M.; Donohue, D.M. Chemotherapy of lymphoma with mechlorethamine and vinblastine. *Arch. Intern.* **1973**, *131*, 407–417. [CrossRef]
27. Jacobs, E.M.; Peters, F.C.; Luce, J.K.; Zippin, C.; Wood, D.A. Mechlorethamine HCl and cyclophosphamide in the treatment of Hodgkin's disease and the lymphomas. *JAMA* **1968**, *203*, 392–398. [CrossRef]
28. Vonderheid, E.C.; Tan, E.T.; Kantor, A.F.; Shrager, L.; Micaily, B.; Van Scott, E.J. Long-term efficacy, curative potential, and carcinogenicity of topical mechlorethamine chemotherapy in cutaneous T cell lymphoma. *J. Am. Acad. Dermatol.* **1989**, *20*, 416–428. [CrossRef] [PubMed]
29. Mekkey, S.M.; Al-dolaimy, F.; Hussein, U.A.-R.; Younis, S.M.D.; Kadhim, A.J.; Kareem, M.W.A.; Abed, N.K.; Asiri, M.; Alkhayyat, S.; Alsalamy, A.H. Investigation of Drug Delivery of Mechlorethamine (Anticancer Drug) by Si76, C76, Al38N38 Nanocages. *Silicon* **2024**, *16*, 585–592. [CrossRef]
30. de Vries Schultink, A.; Suleiman, A.; Schellens, J.; Beijnen, J.; Huitema, A. Pharmacodynamic modeling of adverse effects of anti-cancer drug treatment. *Eur. J. Clin. Pharmacol.* **2016**, *72*, 645–653. [CrossRef]
31. Zhong, Q.; Zee, K.; Rasmussen, K.; McKinley, B.J.; Linger, R.M.; Ray, S.D. Side effects of anti-cancer medications. In *Side Effects of Drugs Annual*; Elsevier: Amsterdam, The Netherlands, 2022; Volume 44, pp. 431–445.
32. Torino, F.; Barnabei, A.; Paragliola, R.M.; Marchetti, P.; Salvatori, R.; Corsello, S.M. Endocrine side-effects of anti-cancer drugs: mAbs and pituitary dysfunction: Clinical evidence and pathogenic hypotheses. *Eur. J. Endocrinol.* **2013**, *169*, R153–R164. [CrossRef] [PubMed]
33. Kashkooli, F.M.; Soltani, M.; Souri, M. Controlled anti-cancer drug release through advanced nano-drug delivery systems: Static and dynamic targeting strategies. *J. Control. Release.* **2020**, *327*, 316–349. [CrossRef] [PubMed]
34. Qin, S.-Y.; Zhang, A.-Q.; Cheng, S.-X.; Rong, L.; Zhang, X.-Z. Drug self-delivery systems for cancer therapy. *Biomaterials* **2017**, *112*, 234–247. [CrossRef] [PubMed]
35. Rashidi, N.; Davidson, M.; Apostolopoulos, V.; Kelley, M.R.; Nurgali, K. Targeted combination nano-drug delivery system to enhance anti-cancer efficacy and reduce side effects. *Cancer Res.* **2024**, *84*, 478. [CrossRef]
36. Xu, H.; Wang, Q.; Fan, G.; Chu, X. Theoretical study of boron nitride nanotubes as drug delivery vehicles of some anticancer drugs. *Theor. Chem. Acc.* **2018**, *137*, 104. [CrossRef]
37. Li, Y.; Xiao, K.; Luo, J.; Lee, J.; Pan, S.; Lam, K.S. A novel size-tunable nanocarrier system for targeted anticancer drug delivery. *J. Control. Release* **2010**, *144*, 314–323. [CrossRef]
38. Zhang, H.; Fan, T.; Chen, W.; Li, Y.; Wang, B. Recent advances of two-dimensional materials in smart drug delivery nano-systems. *Bioact. Mater.* **2020**, *5*, 1071–1086. [CrossRef]
39. Molaei, M.J. Two-dimensional (2D) materials beyond graphene in cancer drug delivery, photothermal and photodynamic therapy, recent advances and challenges ahead: A review. *J. Drug Deliv. Sci. Technol.* **2021**, *61*, 101830. [CrossRef]
40. Gangrade, A.; Mandal, B.B. Drug delivery of anticancer drugs from injectable 3D porous silk scaffold for prevention of gastric cancer growth and recurrence. *ACS Biomater. Sci. Eng.* **2020**, *6*, 6195–6206. [CrossRef]
41. Shi, K.; Aviles-Espinosa, R.; Rendon-Morales, E.; Woodbine, L.; Maniruzzaman, M.; Nokhodchi, A. Novel 3D printed device with integrated macroscale magnetic field triggerable anti-cancer drug delivery system. *Colloids Surf. B Biointerfaces* **2020**, *192*, 111068. [CrossRef]

42. Weng, Q.; Wang, B.; Wang, X.; Hanagata, N.; Li, X.; Liu, D.; Wang, X.; Jiang, X.; Bando, Y.; Golberg, D. Highly water-soluble, porous, and biocompatible boron nitrides for anticancer drug delivery. *ACS Nano* **2014**, *8*, 6123–6130. [CrossRef] [PubMed]
43. Zhang, Z.; Yan, W.; Ji, Y. A novel manganese dioxide-based drug delivery strategy via in situ coating γ-polyglutamic acid/cisplatin for intelligent anticancer therapy. *J. Mater. Chem. B* **2023**, *11*, 667–674. [CrossRef]
44. Chen, H.; Liu, T.; Su, Z.; Shang, L.; Wei, G. 2D transition metal dichalcogenide nanosheets for photo/thermo-based tumor imaging and therapy. *Nanoscale Horiz.* **2018**, *3*, 74–89. [CrossRef] [PubMed]
45. Chandrakala, V.; Aruna, V.; Angajala, G. Review on metal nanoparticles as nanocarriers: Current challenges and perspectives in drug delivery systems. *Emergent Mater.* **2022**, *5*, 1593–1615. [CrossRef]
46. Wu, M.; Yang, J.; Ye, T.; Wang, B.; Tang, Y.; Ying, X. Efficient Drug Delivery of Ti3C2T x MXenes for Synergistic Treatment of Human Hypopharyngeal Squamous Cell Carcinoma. *ACS Appl. Mater. Interfaces* **2023**, *15*, 29939–29947. [CrossRef] [PubMed]
47. Liang, W.; Luo, X. Theoretical studies of MoS2 and phosphorene drug delivery for antituberculosis drugs. *J. Phys. Chem. C* **2020**, *124*, 8279–8287. [CrossRef]
48. Wang, G.; Li, R.; Parseh, B.; Du, G. Prospects and challenges of anticancer agents' delivery via chitosan-based drug carriers to combat breast cancer: A review. *Carbohydr. Polym.* **2021**, *268*, 118192. [CrossRef]
49. Vuong, B.X.; Hajali, N.; Asadi, A.; Baqer, A.A.; Hachim, S.K.; Canli, G. Drug delivery assessment of an iron-doped fullerene cage towards thiotepa anticancer drug. *Inorg. Chem. Commun.* **2022**, *141*, 109558. [CrossRef]
50. Gong, P.; Du, J.; Wang, D.; Cao, B.; Tian, M.; Wang, Y.; Sun, L.; Ji, S.; Liu, Z. Fluorinated graphene as an anticancer nanocarrier: An experimental and DFT study. *J. Mater. Chem. B* **2018**, *6*, 2769–2777. [CrossRef]
51. Guven, A.; Villares, G.J.; Hilsenbeck, S.G.; Lewis, A.; Landua, J.D.; Dobrolecki, L.E.; Wilson, L.J.; Lewis, M.T. Carbon nanotube capsules enhance the in vivo efficacy of cisplatin. *Acta Biomater.* **2017**, *58*, 466–478. [CrossRef]
52. Guo, X.-L.; Kang, X.-X.; Wang, Y.-Q.; Zhang, X.-J.; Li, C.-J.; Liu, Y.; Du, L.-B. Co-delivery of cisplatin and doxorubicin by covalently conjugating with polyamidoamine dendrimer for enhanced synergistic cancer therapy. *Acta Biomater.* **2019**, *84*, 367–377. [CrossRef] [PubMed]
53. Farooq, M.A.; Aquib, M.; Farooq, A.; Haleem Khan, D.; Joelle Maviah, M.B.; Sied Filli, M.; Kesse, S.; Boakye-Yiadom, K.O.; Mavlyanova, R.; Parveen, A. Recent progress in nanotechnology-based novel drug delivery systems in designing of cisplatin for cancer therapy: An overview. *Artif. Cells Nanomed. Biotechnol.* **2019**, *47*, 1674–1692. [CrossRef] [PubMed]
54. Zhang, Y.; Sun, S.; Wu, Y.; Chen, F. Emerging Roles of Graphitic Carbon Nitride-based Materials in Biomedical Applications. *ACS Biomater. Sci. Eng.* **2024**, *10*, 4645–4661. [CrossRef] [PubMed]
55. Ning, X.-F.; Zhu, Y.-Q.; Sun, H.; Yang, Y.; Liu, M.-X. The Latest Applications of Carbon-Nitride-Based Materials for Combination Treatment of Cancer. *ACS Appl. Mater. Interfaces* **2024**, *16*, 64410–64423. [CrossRef]
56. Zaboli, A.; Raissi, H.; Farzad, F.; Hashemzadeh, H. Assessment of adsorption behavior of 5-fluorouracil and pyrazinamide on carbon nitride and folic acid-conjugated carbon nitride nanosheets for targeting drug delivery. *J. Mol. Liq.* **2020**, *301*, 112435. [CrossRef]
57. Ahsan, F.; Yar, M.; Gulzar, A.; Ayub, K. Therapeutic potential of C2N as targeted drug delivery system for fluorouracil and nitrosourea to treat cancer: A theoretical study. *J. Nanostruct. Chem.* **2023**, *13*, 89–102. [CrossRef]
58. Pourmadadi, M.; Rahmani, E.; Eshaghi, M.M.; Shamsabadipour, A.; Ghotekar, S.; Rahdar, A.; Ferreira, L.F.R. Graphitic carbon nitride (g-C3N4) synthesis methods, surface functionalization, and drug delivery applications: A review. *J. Drug Deliv. Sci. Technol.* **2023**, *79*, 104001. [CrossRef]
59. Wang, X.; Liu, S.; Wang, J.; Liu, Y.; Guan, S.; Zhang, T. Spherical g-C3N4@ PDA nanocarrier for synergistic chemo-photothermal tumor therapy. *J. Photochem. Photobiol. A Chem.* **2024**, *454*, 115736. [CrossRef]
60. Asghar, S.; Roudgar-Amoli, M.; Alizadeh, A.; Shariatinia, Z. Water purification through adsorption of organic pollutant onto novel and effective phosphorus-containing g-C3N4/FeMo0. 5O3 nanocomposites. *Water Air Soil Pollut.* **2023**, *234*, 43. [CrossRef]
61. Singh, J.A.; Overbury, S.H.; Dudney, N.J.; Li, M.; Veith, G.M. Gold nanoparticles supported on carbon nitride: Influence of surface hydroxyls on low temperature carbon monoxide oxidation. *ACS Catal.* **2012**, *2*, 1138–1146. [CrossRef]
62. Ou, H.; Ning, S.; Zhu, P.; Chen, S.; Han, A.; Kang, Q.; Hu, Z.; Ye, J.; Wang, D.; Li, Y. Carbon nitride photocatalysts with integrated oxidation and reduction atomic active centers for improved CO2 conversion. *Angew. Chem. Int. Ed.* **2022**, *61*, e202206579. [CrossRef] [PubMed]
63. Liang, H.; Wang, A.; Cheng, R.; Tian, X.; Jing, S.; Tsiakaras, P. Efficient photocatalytic H2O2 production ability of a novel graphitic carbon nitride/carbon composites under visible light. *Small* **2023**, *19*, 2303813. [CrossRef]
64. Peng, G.; Wu, J.; Wang, M.; Niklas, J.; Zhou, H.; Liu, C. Nitrogen-defective polymeric carbon nitride nanolayer enabled efficient electrocatalytic nitrogen reduction with high faradaic efficiency. *Nano Lett.* **2020**, *20*, 2879–2885. [CrossRef]
65. Tan, L.; Nie, C.; Ao, Z.; Sun, H.; An, T.; Wang, S. Novel two-dimensional crystalline carbon nitrides beyond gC 3 N 4: Structure and applications. *J. Meter. Chem. A* **2021**, *9*, 17–33. [CrossRef]

66. Shamim, M.; Perveen, M.; Nazir, S.; Hussnain, M.; Mehmood, R.; Khan, M.I.; Iqbal, J. DFT study of therapeutic potential of graphitic carbon nitride (g-C3N4) as a new drug delivery system for carboplatin to treat cancer. *J. Mol. Liq.* **2021**, *331*, 115607. [CrossRef]
67. Perveen, M.; Aslam, F.; Nazir, S.; Khan, M.I.; Zahra, G.; Iqbal, J. DFT study of therapeutic potential of graphitic carbon nitride as a carrier for controlled release of melphalan: An anticancer drug. *J. Mol. Model.* **2022**, *28*, 359. [CrossRef] [PubMed]
68. Xu, X.; Zhang, X.; He, H.; Dai, L.; Hu, J.; Si, C. Graphitic carbon nitride enters the scene: A promising versatile tool for biomedical applications. *Langmuir* **2024**, *40*, 15389–15406. [CrossRef]
69. Bian, C.; Wang, Y.; Yi, Y.; Shao, S.; Sun, P.; Xiao, Y.; Wang, W.; Dong, X. Enhanced photocatalytic activity of S-doped graphitic carbon nitride hollow microspheres: Synergistic effect, high-concentration antibiotic elimination and antibacterial behavior. *J. Colloid Interface Sci.* **2023**, *643*, 256–266. [CrossRef]
70. Dong, J.; Zhao, Y.; Wang, K.; Chen, H.; Liu, L.; Sun, B.; Yang, M.; Sun, L.; Wang, Y.; Yu, X. Fabrication of graphitic carbon nitride quantum dots and their application for simultaneous fluorescence imaging and pH-responsive drug release. *ChemistrySelect* **2018**, *3*, 12696–12703. [CrossRef]
71. Asif, K.; Perveen, M.; Khera, R.A.; Nazir, S.; Ayub, A.R.; Asif, T.; Shabbir, M.; Iqbal, J. Computational and theoretical study of graphitic carbon nitride (g-C3N4) as a drug delivery carrier for lonidamine drug to treat cancer. *Comput. Theor. Chem.* **2021**, *1206*, 113459. [CrossRef]
72. Li, X. Aluminium nitride as an efficient catalyst in the synthesis of some chromeno [4, 3-b] chromenes and potential nanocarrier for delivery of flutamide. *Chem. Pap.* **2024**, *78*, 1157–1166. [CrossRef]
73. Chen, W.; Liu, J.; Wang, Y.; Jiang, C.; Yu, B.; Sun, Z.; Lu, L. A C5N2 nanoparticle based direct nucleus delivery platform for synergistic cancer therapy. *Angew. Chem.* **2019**, *131*, 6356–6360. [CrossRef]
74. Karimi, M.; Solati, N.; Amiri, M.; Mirshekari, H.; Mohamed, E.; Taheri, M.; Hashemkhani, M.; Saeidi, A.; Estiar, M.A.; Kiani, P. Carbon nanotubes part I: Preparation of a novel and versatile drug-delivery vehicle. *Expert Opin. Drug Deliv.* **2015**, *12*, 1071–1087. [CrossRef]
75. Watermann, A.; Brieger, J. Mesoporous silica nanoparticles as drug delivery vehicles in cancer. *Nanomater.* **2017**, *7*, 189. [CrossRef]
76. Sun, C.-Y.; Qin, C.; Wang, X.-L.; Su, Z.-M. Metal-organic frameworks as potential drug delivery systems. *Expert Opin. Drug Deliv.* **2013**, *10*, 89–101. [CrossRef] [PubMed]
77. Liu, J.; Cui, L.; Losic, D. Graphene and graphene oxide as new nanocarriers for drug delivery applications. *Acta Biomater.* **2013**, *9*, 9243–9257. [CrossRef] [PubMed]
78. Garriga, R.; Herrero-Continente, T.; Palos, M.; Cebolla, V.L.; Osada, J.; Muñoz, E.; Rodríguez-Yoldi, M.J. Toxicity of carbon nanomaterials and their potential application as drug delivery systems: In vitro studies in Caco-2 and MCF-7 cell lines. *Nanomaterials* **2020**, *10*, 1617. [CrossRef]
79. Sayers, E.W.; Beck, J.; Bolton, E.E.; Brister, J.R.; Chan, J.; Connor, R.; Feldgarden, M.; Fine, A.M.; Funk, K.; Hoffman, J. Database resources of the National Center for Biotechnology Information in 2025. *Nucleic Acids Res.* **2024**, *53*, D20. [CrossRef] [PubMed]
80. Qi, S.; Jin, Z.; Hou, Y.; Li, C.; Wang, X.; Zhou, Q. Converting an Almost Noncytotoxic Ru (II) Complex with Photolabile Ligands into a Highly Efficient PACT Agent. *Part. Part. Syst. Charact.* **2021**, *38*, 2100193. [CrossRef]
81. Chen, W.; Sun, Z.; Jiang, C.; Sun, W.; Yu, B.; Wang, W.; Lu, L. An All-in-One Organic Semiconductor for Targeted Photoxidation Catalysis in Hypoxic Tumor. *Angew. Chem.* **2021**, *133*, 16777–16784. [CrossRef]
82. Rosenkranz, A.; Ulasov, A.; Slastnikova, T.; Khramtsov, Y.V.; Sobolev, A. Use of intracellular transport processes for targeted drug delivery into a specified cellular compartment. *Biochemistry (Moscow)* **2014**, *79*, 928–946. [CrossRef] [PubMed]
83. Xiang, S.; Liu, J.; Han, G.; Zhang, W.; Long, Y.; Deng, Y.; Wang, B.; Weng, Q. Design of red-emitting 1D zinc coordination polymer for targeted drug delivery to nucleus. *Chem. Eng. J.* **2023**, *470*, 144177. [CrossRef]
84. Dennington, R.; Keith, T.A.; Millam, J.M. *GaussView, Version. 6.0*; Semichem Inc.: Shawnee Mission, KS, USA, 2016.
85. Yaghoubi, A.; Ramazani, A. Using Gaussian and GaussView software for effective teaching of chemistry by drawing molecules. *Res. Chem. Educ.* **2024**, *6*, 69–90. [CrossRef]
86. Frisch, M.J.; Trucks, G.W.; Schlegel, H.B.; Scuseria, G.E.; Robb, M.A.; Cheeseman, J.R.; Scalmani, G.; Barone, V.; Petersson, G.A.; Nakatsuji, H.; et al. *Gaussian, Version 16 Rev. C.01*; Gaussian, Inc.: Wallingford, CT, USA, 2016.
87. Adamo, C.; Barone, V. Toward reliable density functional methods without adjustable parameters: The PBE0 model. *J. Chem. Phys.* **1999**, *110*, 6158–6170. [CrossRef]
88. Marsman, M.; Paier, J.; Stroppa, A.; Kresse, G. Hybrid functionals applied to extended systems. *J. Phys. Condens. Matter* **2008**, *20*, 064201. [CrossRef]
89. Adamo, C.; Cossi, M.; Scalmani, G.; Barone, V. Accurate static polarizabilities by density functional theory: Assessment of the PBE0 model. *Chem. Phys. Lett.* **1999**, *307*, 265–271. [CrossRef]
90. Melissen, S.; Le Bahers, T.; Steinmann, S.N.; Sautet, P. Relationship between Carbon Nitride Structure and Exciton Binding Energies: A DFT Perspective. *J. Physs. Chem. C* **2015**, *119*, 25188–25196. [CrossRef]

91. Tuma, C.; Boese, A.D.; Handy, N.C. Predicting the binding energies of H-bonded complexes: A comparative DFT study. *Phys. Chem. Chem. Phys.* **1999**, *1*, 3939–3947. [CrossRef]
92. Lin, T.-J.; Chiu, C.-c. Influence of nonmetal dopants on charge separation of graphitic carbon nitride by time-dependent density functional theory. *Phys. Chem. Chem. Phys.* **2020**, *22*, 647–657. [CrossRef]
93. Veccham, S.P.; Head-Gordon, M. Density functionals for hydrogen storage: Defining the H2Bind275 test set with ab initio benchmarks and assessment of 55 functionals. *J. Chem. Theory Comput.* **2020**, *16*, 4963–4982. [CrossRef]
94. Galimov, E.R.; Kostjukov, V.V. Computational analysis of photoisomerization of unsubstituted spirooxazine by TD-DFT: Solvent effect and functional choice. *Theor. Chem. Acc.* **2023**, *143*, 2. [CrossRef]
95. Xu, H.; Tu, X.; Fan, G.; Wang, Q.; Wang, X.; Chu, X. Adsorption properties study of boron nitride fullerene for the application as smart drug delivery agent of anti-cancer drug hydroxyurea by density functional theory. *J. Mol. Liq.* **2020**, *318*, 114315. [CrossRef]
96. Barman, R.; Bej, R.; Dey, P.; Ghosh, S. Cisplatin-conjugated polyurethane capsule for dual drug delivery to a cancer cell. *ACS Appl. Mater. Interfaces* **2023**, *15*, 25193–25200. [CrossRef]
97. Chu, Y.-C.; Lin, T.-J.; Lin, Y.-R.; Chiu, W.-L.; Nguyen, B.-S.; Hu, C. Influence of P,S,O-Doping on g-C3N4 for hydrogel formation and photocatalysis: An experimental and theoretical study. *Carbon* **2020**, *169*, 338–348. [CrossRef]
98. Ibarra-Rodríguez, M.; Sánchez, M. Adsorption of metformin on graphitic carbon nitride functionalized with metals of group 1–3 (Li, Na, K, Be, Mg, Ca, B, Al, and Ga), DFT calculations. *Comput. Theor. Chem.* **2022**, *1207*, 113532. [CrossRef]
99. Ibarra-Rodríguez, M.; Sánchez, M. Graphitic carbon nitride functionalized with four boron atoms for adsorption and separation of CO2/CH4: DFT calculations. *Adsorption* **2020**, *26*, 597–605. [CrossRef]
100. Ibarra-Rodríguez, M.; Sánchez, M. Adsorption of H2, N2, CO, H2S, NH3, SO2 and CH4 on Li-functionalized graphitic carbon nitride investigated by density functional theory. *Bull. Mater. Sci.* **2020**, *43*, 144. [CrossRef]
101. Gorai, D.K.; Kundu, T.K. Platinum-silicon doped graphitic carbon nitride: A first principle calculation. *Phys. B Condens. Matter* **2022**, *627*, 413547. [CrossRef]
102. Pauly, M.; White, E.; Deegbey, M.; Fosu, E.A.; Keller, L.; McGuigan, S.; Dianat, G.; Gabilondo, E.; Wong, J.C.; Murphey, C.G.E.; et al. Coordination of copper within a crystalline carbon nitride and its catalytic reduction of CO2. *Dalton Trans.* **2024**, *53*, 6779–6790. [CrossRef]
103. Ali, B.; Siddique, S.A.; Ahmed Siddique, M.B.; Ullah, S.; Ali, M.A.; Rauf, A.; Kamran, M.A.; Arshad, M. Insight on the structural, electronic and optical properties of Zn, Ga-doped/dual-doped graphitic carbon nitride for visible-light applications. *J. Mol. Graph. Model.* **2023**, *125*, 108603. [CrossRef]
104. Kresse, G.; Furthmüller, J. Efficiency of ab-initio total energy calculations for metals and semiconductors using a plane-wave basis set. *Comput. Mater. Sci.* **1996**, *6*, 15–50. [CrossRef]
105. Liu, W.-W.; Niu, S.-T.; Xu, Z.-Q.; Zou, R.; Cui, C.-Y.; Lei, Y.-X.; Zhang, X.-B.; Ran, F. Highly-dispersed nickel on 2D graphitic carbon nitrides (g-C3N4) for facilitating reaction kinetics of lithium-sulfur batteries. *Appl. Surf. Sci.* **2023**, *609*, 155327. [CrossRef]
106. Grimme, S.; Ehrlich, S.; Goerigk, L. Effect of the damping function in dispersion corrected density functional theory. *J. Comput. Chem.* **2011**, *32*, 1456–1465. [CrossRef]
107. Grimme, S.; Antony, J.; Ehrlich, S.; Krieg, H. A consistent and accurate ab initio parametrization of density functional dispersion correction (DFT-D) for the 94 elements H-Pu. *J. Chem. Phys.* **2010**, *132*, 154104. [CrossRef]
108. Legault, C. *CYLview, Version 1.0 b*; Université de Sherbrooke: Sherbrooke, QC, Canada, 2009.
109. O'Boyle, N.M.; Tenderholt, A.L.; Langner, K.M. cclib: A library for package-independent computational chemistry algorithms. *J Comput. Chem.* **2008**, *29*, 839–845. [CrossRef]
110. Lu, T.; Chen, F. Multiwfn: A multifunctional wavefunction analyzer. *J Comput. Chem.* **2012**, *33*, 580–592. [CrossRef]
111. Humphrey, W.; Dalke, A.; Schulten, K. VMD: Visual molecular dynamics. *J. Mol. Graph.* **1996**, *14*, 33–38. [CrossRef]
112. Contreras-García, J.; Johnson, E.R.; Keinan, S.; Chaudret, R.; Piquemal, J.-P.; Beratan, D.N.; Yang, W. NCIPLOT: A Program for Plotting Noncovalent Interaction Regions. *J. Chem. Theory Comput.* **2011**, *7*, 625–632. [CrossRef] [PubMed]
113. Vargas, R.; Garza, J.; Martínez, A.; Ibarra, I.A. Computational tools to study non-covalent interactions and confinement effects in chemical systems. *Chem. Commun.* **2024**, *60*, 3008–3018. [CrossRef]
114. Hajji, M.; Abad, N.; Habib, M.A.; Elmgirhi, S.M.H.; Guerfel, T. Computational chemistry methods for modelling non-covalent interactions and chemical reactivity—An overview. *J. Indian Chem. Soc.* **2021**, *98*, 100208. [CrossRef]
115. Popelier, P.L.A. The QTAIM Perspective of Chemical Bonding. In *The Chemical Bond*; John Wiley & Sons: Hoboken, NJ, USA, 2014; pp. 271–308.
116. Kumar, P.S.V.; Raghavendra, V.; Subramanian, V. Bader's Theory of Atoms in Molecules (AIM) and its Applications to Chemical Bonding. *J. Chem. Sci.* **2016**, *128*, 1527–1536. [CrossRef]
117. Foroutan-Nejad, C.; Shahbazian, S.; Marek, R. Toward a Consistent Interpretation of the QTAIM: Tortuous Link between Chemical Bonds, Interactions, and Bond/Line Paths. *Chem. A Eur. J.* **2014**, *20*, 10140–10152. [CrossRef] [PubMed]
118. Wick, C.R.; Clark, T. On bond-critical points in QTAIM and weak interactions. *J. Mol. Model.* **2018**, *24*, 142. [CrossRef] [PubMed]

119. Bader, R.F. Comment on: Revisiting the variational nature of the quantum theory of atoms in molecules. *Chem. Phys. Lett.* **2006**, *426*, 226–228. [CrossRef]
120. Phillips, J.C. Generalized Koopmans' Theorem. *Phys. Rev.* **1961**, *123*, 420–424. [CrossRef]
121. Hackett, J.C. Chemical Reactivity Theory: A Density Functional View. *J. Am. Chem. Soc.* **2010**, *132*, 7558. [CrossRef]
122. Parr, R.G.; Szentpály, L.v.; Liu, S. Electrophilicity index. *J. Am. Chem. Soc.* **1999**, *121*, 1922–1924. [CrossRef]
123. Bendjeddou, A.; Abbaz, T.; Gouasmia, A.; Villemin, D. Quantum chemical studies on molecular structure and reactivity descriptors of some P-nitrophenyl tetrathiafulvalenes by density functional theory (DFT). *Acta Chim. Pharm. Indica* **2016**, *6*, 32–44.
124. de Miranda, D.B.; Quintal, S.; Ferreira, G.B. Electronic analysis of n-propyl xanthate complexes with group 12 metals: A theoretical–experimental study. *J. Mol. Model.* **2024**, *30*, 163. [CrossRef]
125. Shilpa, D.; Sadasivam, K.; Thirumoorthy, M. Topology analysis of six phytochemicals through ELF and LOL basins–A DFT study. *Indian J. Chem. (IJC)* **2023**, *62*, 1171–1177.
126. Jumabaev, A.; Koyambo-Konzapa, S.-J.; Hushvaktov, H.; Absanov, A.; Khudaykulov, B.; Holikulov, U.; Ernazarov, Z.; Issaoui, N.; Al-Dossary, O.M.; Nsangou, M. Intermolecular interactions in water and ethanol solution of ethyl acetate: Raman, DFT, MEP, FMO, AIM, NCI-RDG, ELF, and LOL analyses. *J. Mol. Model.* **2024**, *30*, 349. [CrossRef] [PubMed]
127. Weinhold, F. Natural bond orbital analysis: A critical overview of relationships to alternative bonding perspectives. *J. Comput. Chem.* **2012**, *33*, 2363–2379. [CrossRef] [PubMed]
128. Koch, D.; Pavanello, M.; Shao, X.; Ihara, M.; Ayers, P.W.; Matta, C.F.; Jenkins, S.; Manzhos, S. The Analysis of Electron Densities: From Basics to Emergent Applications. *Chem. Rev.* **2024**, *124*, 12661–12737. [CrossRef]
129. Leppert, J.; Urbinati, C.R.; Häfner, S.; Ohlenschläger, O.; Swanson, M.S.; Görlach, M.; Ramachandran, R. Identification of NH...N hydrogen bonds by magic angle spinning solid state NMR in a double-stranded RNA associated with myotonic dystrophy. *Nucleic Acids Res.* **2004**, *32*, 1177–1183. [CrossRef] [PubMed]
130. Pakiari, A.; Eskandari, K. The chemical nature of very strong hydrogen bonds in some categories of compounds. *J. Mol. Struct. THEOCHEM* **2006**, *759*, 51–60. [CrossRef]
131. Grabowski, S.J. Hydrogen Bond—Definitions, Criteria of Existence and Various Types. In *Understanding Hydrogen Bonds*; The Royal Society of Chemistry: London, UK, 2020.
132. Schiemenz, G.P. The sum of van der Waals radii–A pitfall in the search for bonding. *Z. Naturforschung B* **2007**, *62*, 235–243. [CrossRef]
133. Kaviani, S.; Shahab, S.; Sheikhi, M.; Potkin, V.; Zhou, H. A DFT study of Se-decorated B12N12 nanocluster as a possible drug delivery system for ciclopirox. *Comput. Theor. Chem.* **2021**, *1201*, 113246. [CrossRef]
134. Nayini, M.M.R.; Sayadian, H.; Razavipour, N.; Rezazade, M. Chemical-sensing of Amphetamine drug by inorganic AlN nano-cage: A DFT/TDDFT study. *Inorg. Chem. Commun.* **2020**, *121*, 108237. [CrossRef]
135. Wang, L.; Liu, X.; Ji, L.; Luo, Q.; Duan, Y.; An, J.; Chen, X.; Zhang, Y.; Ren, J.; Wang, D. Resin with short-range π-π stacking aggregates for an efficient photocatalyst. *Chem. Eng. J.* **2022**, *433*, 134502. [CrossRef]
136. Tomasi, J.; Mennucci, B.; Cammi, R. Quantum mechanical continuum solvation models. *Chem. Rev.* **2005**, *105*, 2999–3094. [CrossRef]
137. Kalhor, S.; Fattahi, A. Combinatorial MD/QM studies to develop novel ionic liquid-based anticancer drug delivery systems with aminium derived from carbohydrates as cationic components. *Sci. Rep.* **2024**, *14*, 28980. [CrossRef] [PubMed]
138. Marenich, A.V.; Cramer, C.J.; Truhlar, D.G. Universal Solvation Model Based on Solute Electron Density and on a Continuum Model of the Solvent Defined by the Bulk Dielectric Constant and Atomic Surface Tensions. *J. Phys. Chem. B* **2009**, *113*, 6378–6396. [CrossRef] [PubMed]
139. Oğuz, I.C.; Vassetti, D.; Labat, F. Assessing the performances of different continuum solvation models for the calculation of hydration energies of molecules, polymers and surfaces: A comparison between the SMD, VASPsol and FDPB models. *Theor. Chem. Acc.* **2021**, *140*, 99. [CrossRef]
140. Gwee, E.S.; Seeger, Z.L.; Appadoo, D.R.; Wood, B.R.; Izgorodina, E.I. Influence of DFT Functionals and Solvation Models on the Prediction of Far-Infrared Spectra of Pt-Based Anticancer Drugs: Why Do Different Complexes Require Different Levels of Theory? *ACS Omega* **2019**, *4*, 5254–5269. [CrossRef]
141. Zafar, A.; Reynisson, J. Hydration free energy as a molecular descriptor in drug design: A feasibility study. *Mol. Inform.* **2016**, *35*, 207–214. [CrossRef] [PubMed]
142. Bibi, S.; Ur-Rehman, S.; Khalid, L.; Bhatti, I.A.; Bhatti, H.N.; Iqbal, J.; Bai, F.Q.; Zhang, H.-X. Investigation of the adsorption properties of gemcitabine anticancer drug with metal-doped boron nitride fullerenes as a drug-delivery carrier: A DFT study. *RSC Adv.* **2022**, *12*, 2873–2887. [CrossRef] [PubMed]
143. Dong, S.; Gong, Y.; Zeng, Z.; Chen, S.; Ye, J.; Wang, Z.; Dionysiou, D.D. Dissolved organic matter promotes photocatalytic degradation of refractory organic pollutants in water by forming hydrogen bonding with photocatalyst. *Water Res.* **2023**, *242*, 120297. [CrossRef] [PubMed]

144. Lu, D.; Chen, Y.; Lu, Z.; Ma, L.; Tao, Q.; Li, Z.; Kong, L.; Liu, L.; Yang, X.; Ding, S. Monolithic three-dimensional tier-by-tier integration via van der Waals lamination. *Nature* **2024**, *630*, 340–345. [CrossRef]
145. Liu, Z.; Chen, K.; Davis, C.; Sherlock, S.; Cao, Q.; Chen, X.; Dai, H. Drug delivery with carbon nanotubes for in vivo cancer treatment. *Cancer Res.* **2008**, *68*, 6652–6660. [CrossRef]
146. Saikia, N. Functionalized carbon nanomaterials in drug delivery: Emergent perspectives from application. In *Novel Nanomaterials—Synthesis and Applications*; IntechOpen: London, UK, 2018; pp. 231–255.
147. Lee, Y.; Kwon, D.-G.; Kim, G.; Kwon, Y.-K. Ab initio study of aspirin adsorption on single-walled carbon and carbon nitride nanotubes. *Phys. Chem. Chem. Phys.* **2017**, *19*, 8076–8081. [CrossRef]

Disclaimer/Publisher's Note: The statements, opinions and data contained in all publications are solely those of the individual author(s) and contributor(s) and not of MDPI and/or the editor(s). MDPI and/or the editor(s) disclaim responsibility for any injury to people or property resulting from any ideas, methods, instructions or products referred to in the content.